Petroleum Science 22 (2025) 4933–4953

Contents lists available at ScienceDirect

Petroleum Science

journal homepage: www.keaipublishing.com/en/journals/petroleum-science

Original Paper

Illitisation impeded the thermal evolution of extractable organic matter: An interpretation of the mineralogy and thermal maturation of early Cambrian source rocks in Yunnan Province, China

Qian-Nan Xu [a,b,d,*], Yan-Ming Zhu [b], Shang-Bin Chen [b], Yu Liu [c], Xiao-Qi Wang [e], Fu-Hua Shang [f], Simon C. George [d]

[a] State Key Laboratory of Submarine Geoscience, Second Institute of Oceanography, Ministry of Natural Resources, Hangzhou, 310012, Zhejiang, China
[b] Key Laboratory of Coalbed Methane Resources and Reservoir Formation Process of the Ministry of Education, China University of Mining and Technology, Xuzhou, 221008, Jiangsu, China
[c] College of Geoscience and Surveying Engineering, China University of Mining & Technology (Beijing), Beijing, 100083, China
[d] School of Natural Sciences, Macquarie University, North Ryde, Sydney, NSW, 2109, Australia
[e] Key Laboratory of Mine Water Resource Utilization of Anhui Higher Education Institute, School of Resources and Civil Engineering, Suzhou University, Suzhou, 234000, Jiangsu, China
[f] Inner Mongolia Engineering Research Center of Geological Technology and Geotechnical Engineering, Inner Mongolia University of Technology, Hohhot, 010051, Inner Mongolia, China

ARTICLE INFO

Article history:
Received 4 January 2025
Received in revised form
25 September 2025
Accepted 3 November 2025
Available online 12 November 2025

Edited by Xi Zhang and Jie Hao

Keywords:
PAH
Thermal alteration
Illite crystallinity
Metamorphism
Diagenesis
GC-MS

ABSTRACT

The degree of thermal alteration of organic matter in sediments is crucial for comprehending the progress of oil and gas generation. The thermal maturity of kerogen, which is a component of the organic matter in source rocks, has been extensively studied in early Cambrian strata in the Yangtze Platform. For example, the gas generation potential of the kerogen was determined to be at a mature to over-mature stage. However, there has been relatively less focus on the extractable organic matter. The recognition of extractable organic matter as a source of secondary gas generation has been made in the context of over-mature sediments. The thermal maturity of extractable organic matter is crucial for its interpretation, as is the mineralogy resulting from burial modification, because of the interaction of mineralogy with maturity. Gas chromatography-mass spectrometry analysis was conducted on aromatic compounds from early Cambrian sediments in Yunnan Province. The aromatic compounds were found to possess a preference for β-substituted isomers that are more thermally stable. The ratios determined from alkylated naphthalenes and phenanthrenes, which are reliant on thermal maturity, provided a consistent distribution throughout the different burial depths. However, alkylated biphenyls and alkylated dibenzothiophenes have variable trends, with anomalously lower thermal maturity in the deeper buried sediments. The interaction of aromatic compounds and clays as a function of thermal modification was tested through the use of scanning electron microscopy, with correlation analysis of temperature-dependent aromatic ratios and clays. The correlation coefficients between an illite-associated ratio and thermally-dependent alkylated biphenyl and dibenzothiophene ratios are above 0.9. Our hypothesis is that the process of illitisation hindered the thermal alteration of alkylated biphenyls and dibenzothiophenes.

1. Introduction

The primary origin of gas and oil in early Cambrian strata is the accumulation of organic matter (OM), which in the Yangtze Platform in China has undergone significant burial and thermal alteration as a result of both depositional and tectonic conditions

* Corresponding author.
E-mail addresses: qiannanx@126.com, qiannanx@sio.org.cn (Q.-N. Xu).
Peer review under the responsibility of China University of Petroleum (Beijing).

https://doi.org/10.1016/j.petsci.2025.11.005

(Fang et al., 2019; Tao et al., 2012; Wu et al., 2022; Yan et al., 2016; Zhao et al., 2018). The OM preserved in early Cambrian sediments is type I kerogen (Awan et al., 2020, 2023; Hu et al., 2012), and was determined to be over-mature in the gas generation window (Awan et al., 2023; Hu et al., 2012; Meng et al., 2024; Tao et al., 2012). There are remarkable productivities of gas exploration drill holes in early Cambrian strata in some regions of the Sichuan Basin (He et al., 2023). The quantity of shale gas production is influenced by the amount and thermal maturity of the OM in the shale, as well as variations in reservoir characteristics. However, the study of the thermal maturity of kerogen and extractable organic matter (EOM) in early Cambrian strata in the Yangtze Platform is less well known, but is important for understanding its molecular characteristics during gas production. The progressive transformation of kerogen in sediments has resulted in the generation of residual EOM phases, such as bitumen (He et al., 2013, 2023; Tiem et al., 2008; Yao et al., 2021). This transformation is a result of geological alteration processes which have induced degradation, polymerisation, condensation, and thermal cracking of the OM (He et al., 2023; Liu et al., 2024; Vandenbroucke and Largeau, 2007). Ultimately, these processes lead to the production of gas or oil. Kerogen has been extensively studied for its significant role in gas production, particularly in relation to thermal maturity (Agrawal and Sharma, 2018; Baruah and Tiwari, 2022; Craddock et al., 2015; Robison et al., 2000; Wang and Zhao, 2020). However, the presence of bitumen may impact a shale's gas production capacity, due to both the effect of bitumen on thermal alteration of kerogen, and the bitumen itself which can also serve as a source of gas generation (George and Harris, 1977; He et al., 2013; Peng et al., 2020; Tiem et al., 2008; Yao et al., 2021). The potential for gas generation from EOM, specifically the creation of methane and hydrocarbon gases, may have been overlooked in Cambrian source rocks.

The EOM in source rocks is a relatively small proportion of the total OM, and potentially could be adsorbed onto clay and kerogen (Kennedy et al., 2002; Vandenbroucke and Largeau, 2007; Zhao et al., 2023). The amount of OM that can generate gas has a positive relationship with the specific surface area of clays (Kennedy et al., 2002), resulting in argillaceous rocks that are favourable for shale gas (Li et al., 2021; Tosca et al., 2010; Weaver, 1959; Zhu et al., 2015). The chemical composition of clay mineral surfaces permits adsorption. Illite and smectite have a tetrahedral-octahedral-tetrahedral layer structure (Brindley and Brown, 1980; Velde and Meunier, 2008). Each adjacent tetrahedral layer has a neutral siloxane surface (Kleber et al., 2015), which provides a strong electrostatic charge to the surface with cations due to a plane of oxygen (Velde and Meunier, 2008; Zhao et al., 2023). This type of surface facilitates the strong attachment of EOM to illite or smectite through cation bridging, van der Waals forces, and hydrogen bonding (Kleber et al., 2015), especially for aromatic hydrocarbons (Ahmat et al., 2016). Nevertheless, it is possible that other relationships between aromatic hydrocarbons and clays have not been taken into consideration, as both of them are modified during thermal maturation. For example, the charge conditions of aromatic hydrocarbons are changed during progressive burial alteration. In the case of thermal alteration and gas generation, the release of CH_3^- from alkylated aromatics has the ability to deplete H^+ and thereby reduce the concentration of free H^+ in the chemical environment of a fine-grained rock. This process may occur simultaneously with the transformation of smectite to illite (Pevear, 1999; Rahman et al., 2017).

There is no unambiguous chemical relationship between aromatic hydrocarbons and clay minerals during thermal alteration, but thermally-dependent aromatic ratios have been extensively studied. Polycyclic aromatic hydrocarbons (PAHs) have conjugated bonds, and undergo various thermal alteration processes such as cyclisation, aromatisation, and demethylation (Craddock et al., 2015; Liu et al., 2024; van Aarssen et al., 1999; Vandenbroucke and Largeau, 2007). The isomeric distribution of alkylated PAHs provides thermal maturity data. Examples in oils and source rocks include alkylated naphthalenes (Alexander et al., 1985, 1994; Asahina and Suzuki, 2018; George et al., 2001; Kruge, 2000; Radke et al., 1982b, 1986; van Aarssen et al., 1999), methylphenanthrenes (Kvalheim et al., 1987; Radke et al., 1982a), alkylated biphenyls (Alexander et al., 1986; Cumbers et al., 1987; George and Ahmed, 2002; Martínez et al., 2020; Ogbesejana et al., 2019), alkyldibenzothiophenes (George and Ahmed, 2002; Radke et al., 1986), and methylated pyrenes (Fang et al., 2015; Kvalheim et al., 1987). These thermal-dependent aromatic ratios have been much used to assess varying thermal maturity of oils and source rocks, although have only been used in limited applications for research on over mature sediments from the early Cambrian (Hall, 2012), and thermal implications of OM during illitisation (Du et al., 2021; Lázaro, 2007; Tannenbaum and Kaplan, 1985; Zhao et al., 2023).

Organic matter-bearing sediments from the early Cambrian in the Yangtze Platform have been investigated as over mature source rocks (Meng et al., 2024; Tao et al., 2012). However, the thermal alteration of aromatic compounds in the EOM, the effect of diagenesis and burial metamorphism on clays, and the interaction of OM and clay minerals during thermal alteration have not been studied in the Yangtze Platform. Here, we analyse a set of OM-bearing early Cambrian sediment samples by gas chromatography-mass spectrometry (GC-MS), X-ray diffraction (XRD), and scanning electron microscopy (SEM) so as to investigate the thermal maturity of the EOM and the burial alteration intensity of the clays. The aim of this work is to assess the interaction of EOM and clays during thermal alteration.

2. Methods

2.1. Organic geochemistry analysis

2.1.1. Sample information and preparation

The borehole was drilled in Zhaotong city in the Yunnan-Guizhou fold belt, which was located in the western part of the Yangtze Platform during the early Cambrian (Fig. 1(a) and (b)). The Yangtze Platform was profoundly affected by oceanic influx from the southeast during the early Cambrian, resulting in diverse palaeographic facies in the eastern part of Yunnan province (Fig. 1(b)). The sediments in the borehole were generally deposited on a palaeographic shelf, with changes from inner shelf to outer shelf and to prodelta conditions over time, due to sea-level fluctuations (Fig. 1(c)). Sample X1 is from the Yu'an shan Formation, which was deposited in prodelta conditions based on fossil evidence (Zhu et al., 2001; Saleh et al., 2022). The sedimentary structures in sample X1 also suggest robust hydrodynamic conditions, with oscillatory-flow ripples at the base, a cross-laminated climbing ripple in the middle, and hummocky cross stratification in the upper part (Fig. 2(a)). Samples X2–X7 are from the Shiyantou Formation and have sedimentary features that indicate a moderate hydrological regime, with parallel bedding in samples X2 and X4 (Fig. 2(b), (d)), irregular ripples in sample X5 (Fig. 2(e)), and very limited discernible sedimentary structures in samples X3, X6, and X7 (Fig. 2(c), (f), (g)). The sampling positions span two different biozones (Fig. 1(c)). Samples X2–X7 were deposited within the small shelly-fauna biozone (Yang et al., 2014), whereas sample X1 was deposited in strata associated with the proliferation of trilobites, sometimes with soft-parts preserved (Steiner et al., 2001). Nevertheless, the redox conditions of the deeper water column

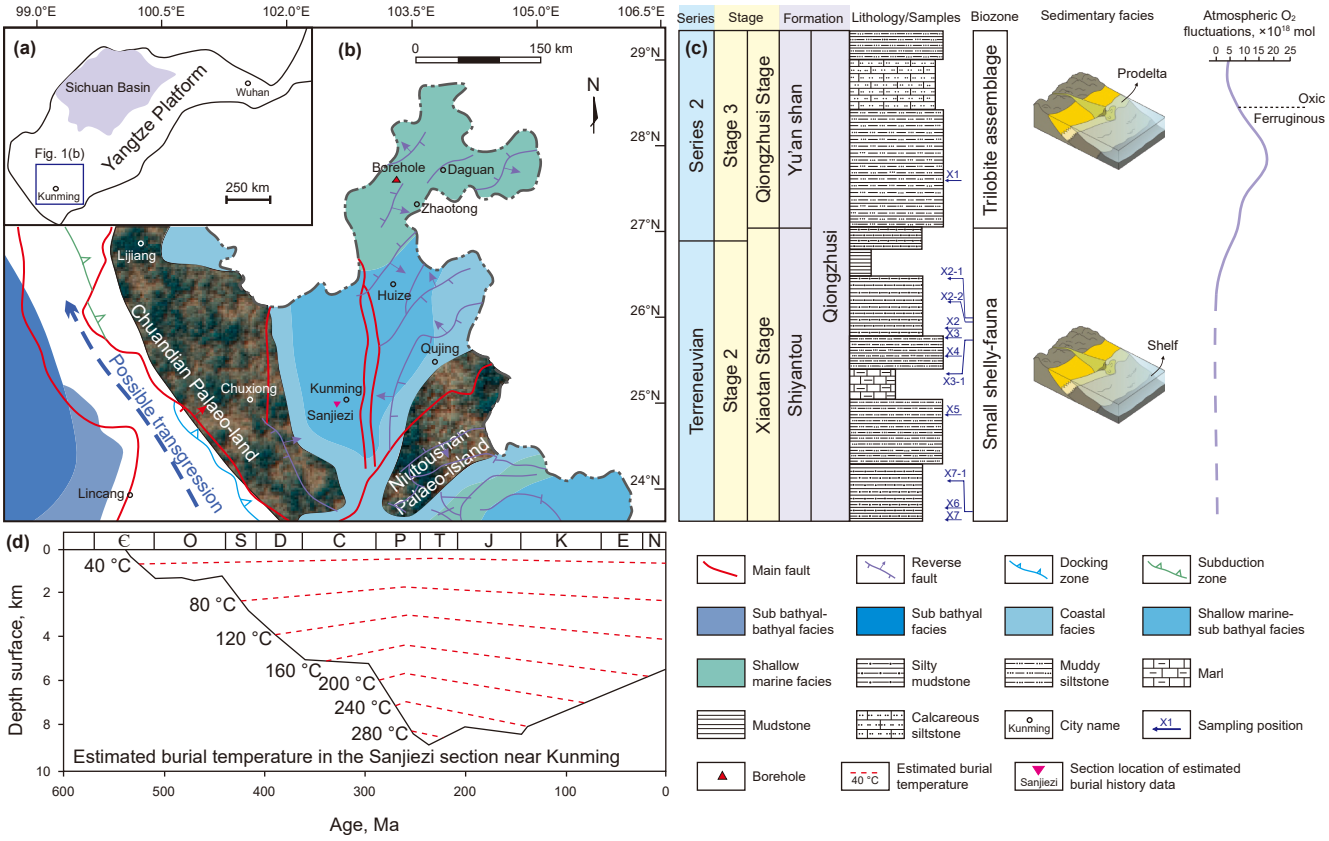

Fig. 1. **(a)** Geographical location of the research area within the Yangtze Platform. **(b)** Sketch of palaeogeographical facies during the early Cambrian (Bureau of geology and mineral resources of Yunnan province, 1990; Zhu et al., 2001; Saleh et al., 2022), principal faults (Ning et al., 2021), and the location of sample drilling in the eastern part of Yunnan province. **(c)** Chronostratigraphy (Zhu et al., 2019, 2021), lithology, sampling position in the borehole, biozones (Steiner et al., 2001; Yang et al., 2014; Lindsay et al., 2015; Saleh et al., 2022; Li et al., 2025), variations in sedimentary facies (Zhu et al., 2001, 2021; Saleh et al., 2022), and atmospheric O_2 fluctuations (Chen et al., 2015; Jiang et al., 2022; Hu et al., 2025) through the Qiongzhusi Formation. **(d)** Burial and thermal history in the middle part of Yunnan province, based on Qiao et al. (2024). Є is the abbreviation of stratigraphic age for Cambrian, O is Ordovician, S is Silurian, D is Devonian, C is Carboniferous, P is Permian, T is Triassic, J is Jurassic, K is Cretaceous, E is Paleogene, and N is Neogene.

were consistently ferruginous (Chen et al., 2015; Jiang et al., 2022; Hu et al., 2025) (Fig. 1(c)), suggesting that OM was preserved under extremely low oxygen levels during initial burial and early diagenesis. The burial history from the southern part of the Sichuan Basin and the Sanjiezi section shows a maximum palaeotemperature of about 280 °C (Qiu et al., 2021; Qiao et al., 2024), which was able to provide sufficient thermal energy for dry gas generation from the kerogen (Fig. 1(d)).

The borehole was drilled with a water-based drilling mud. Core samples were selected and wrapped in foil at room temperature before the experiments. The outer sections of the samples were carefully removed by a rock saw to prevent contamination during sampling, and were retained for XRD analysis. The interior sections were ultrasonicated with a solvent mixture of dichloromethane (DCM) and methanol (9:1, v/v) for 5 min, with the intention of preventing any organic contamination resulting from the slicing process. The interior sections of each sample were subsequently crushed into a fine powder using a ring mill.

2.1.2. Solvent extraction and fractionation

The same 9:1 solvent mixture was used to extract soluble OM from sediments using an Accelerated Solvent Extractor (ASE300). The powdered samples were mixed approximately 1:1 with pre-extracted and combusted sand, so as to improve permeability within the extraction cells and hence increase extraction efficiency. The ASE oven was heated to 100 °C for 5 min, and nitrogen was used to flush all the EOM under a pressure of 1500 psi into a collection bottle. The EOM was purified by treating with activated copper turnings to remove sulfur, and subsequently a 1 mL aliquot from 10 mL was evaporated to dryness and weighed. Extractability was calculated as weight of EOM (mg)/weight of rock (g) (Table 1).

About 10–15 mg of EOM was reduced to a volume of 50 μL by gently blowing under dry nitrogen, and fractionated by column chromatography using a glass Pasteur pipette (100 mm × 5.7 mm i.d.). The pipette was plugged with a small amount of glass wool, and packed with a 45 mm column of silica gel (60–120 μm; approximately 0.6 g). The total hydrocarbons (HCs) were collected by elution with a solution of *n*-hexane/DCM (4:1 v/v, 3 mL), and the polars were eluted with methanol/DCM (1:1 v/v, 3 mL). The total HCs in 50 μL were then fractionated on a new silica column into aliphatic HCs by elution with *n*-hexane (about 2.6 mL), and aromatic HCs by elution with a solution of *n*-hexane/DCM (4:1 v/v, 3.5 mL). Monitoring using ultraviolet light was used to determine the time to switch from collection of aliphatic HCs to aromatic HCs during fractionation.

2.1.3. Gas chromatography-mass spectrometry

Molecular information from the aromatic HC fractions was obtained using an Agilent 6890N GC (DB-5MS column, 60 m × 0.25 mm i.d., film thickness of 0.25 μm) interfaced with an Agilent 5975B mass selective detector, operated with an electron impact of 70 eV. The column oven had an initial temperature of

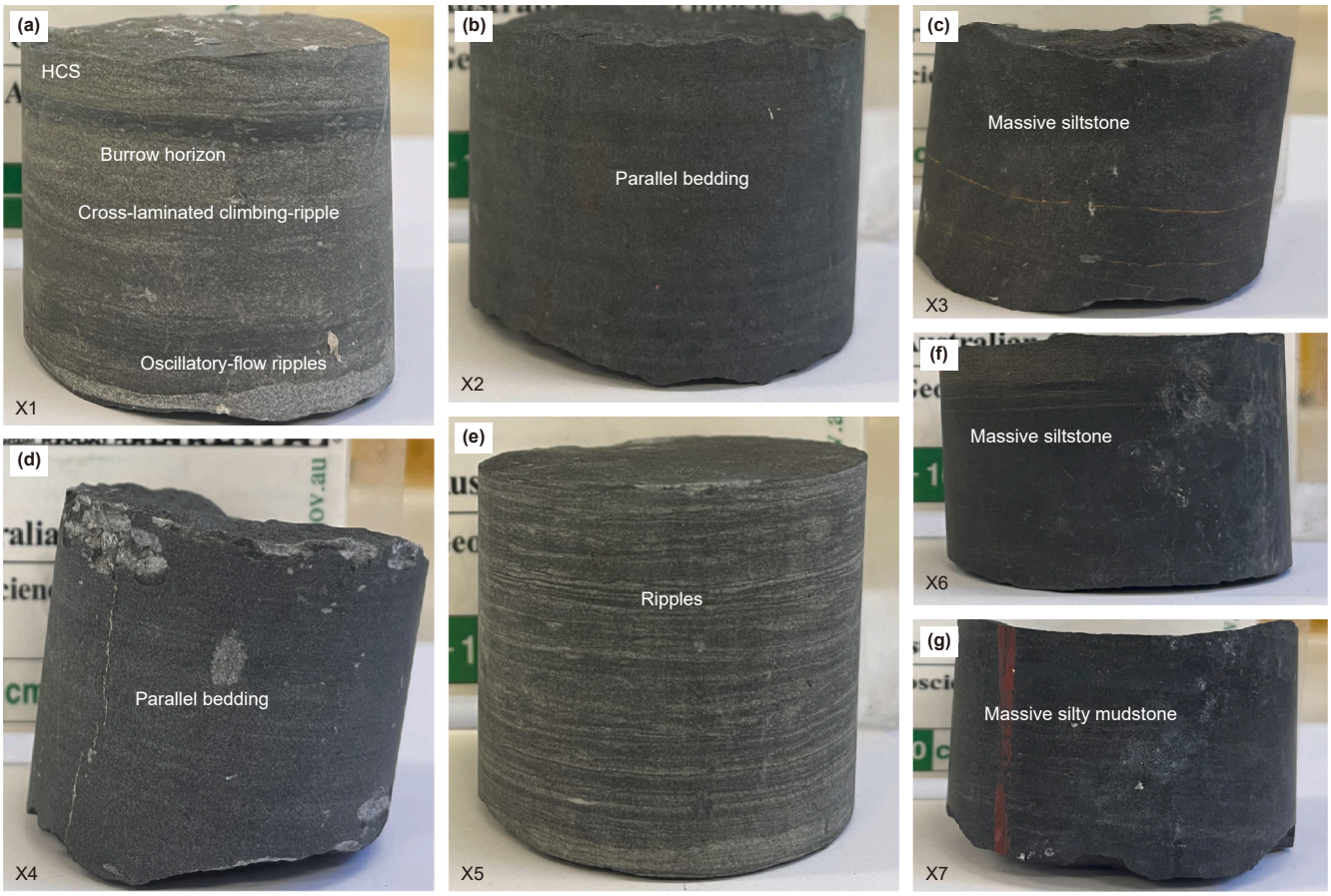

Fig. 2. Photos and sedimentary structures of borehole samples. **(a)** Sample X1; **(b)** sample X2; **(c)** sample X3; **(d)** sample X4; **(e)** sample X5; **(f)** sample X6; **(g)** sample X7. The core has a diameter of 5 cm. HCS = hummocky cross stratification.

Table 1
Core sample depths, list of experiments, and extractability.

Depth, m	Samples	Experiments	Extractability, $\times 10^{-3}$ mg/g
1135.18–1135.58	X1	GC-MS, XRD	127
1217.21–1219.18	X2-1	SEM	nd
1219.58–1222.12	X2-2	SEM	nd
1219.18–1219.48	X2	GC-MS, XRD	112
1225.99–1228.04	X3-1	SEM	nd
1228.04–1228.44	X3	GC-MS, XRD	87
1237.08–1237.48	X4	GC-MS, XRD	52
1271.18–1271.58	X5	GC-MS, XRD	7
1319.18–1319.58	X6	GC-MS, XRD	20
1323.43–1326.08	X7-1	SEM	nd
1326.08–1326.58	X7	GC-MS, XRD	37

GC-MS = gas chromatography-mass spectrometry; SEM = scanning electron microscopy; XRD = X-ray diffraction; nd = not determined.

40 °C with a 2 min hold, and was then programmed at 4 °C/min to 310 °C, with a 40 min hold. The carrier gas was helium at a constant flow of 1.5 mL/min. GC-MS analysis was performed using both scan (*m/z* 50–550) and single ion monitoring modes.

2.1.4. Organic contaminant testing

A series of experiments was conducted to test for organic contaminants from the sampling, packing, and preservation procedures before analysis of the samples was initiated. GC-MS analysis in scan mode was conducted on the EOM from the exterior and interior portions of a core sample, and also on the aromatic and aliphatic fractions from the blanks. In order to assess any organic contaminations from the laboratory, additional scan mode analyses were performed on sand and rotary evaporator procedural blanks. The sand blank was of the sand used for ASE extraction, which was taken through the whole analytical procedure. The rotary evaporator blank was a DCM solution that was specifically used to test the cleanliness of the rotary evaporation system.

2.2. X-ray diffraction

2.2.1. Bulk sediment

Each left-over piece from the outside of the core was ground into a fine powder using a ring mill (Table 1). Ultrapure water and ethanol were utilised to rinse the mill to remove any cross-over contamination from previous samples. All powdered samples were successively loaded into the top-mount of a circular holder, and analysed using an Aeris XRD instrument with Cobalt Kα radiation. A radiation intensity of 0.04 was chosen for the Soller slits in both the incident beam path and the diffracted beam path, operating with a divergence slit of 1/4° and a fixed mask of 20 mm. A goniometer scan was conducted with a step size of 0.02°, covering an angular range of 4°–70°. The scan was performed using a voltage of 40 kV and a current of 15 mA. Each scanning step lasted for 30 s.

All XRD data were analysed using HighScore Plus software. The results were stripped of K-Alpha2 before identification. Each mineral was identified based on *d*-spacings, which are the perpendicular distance between planes in a cubic lattice (Moore,

1972). These *d*-spacings vary among different types of minerals and can be determined through reflection. For example, the *hkl* of [100] quartz typically has a peak at a *d*-spacing of 0.4255 nm, while the *hkl* of [104] calcite is 0.3034 nm. The proportion of identified minerals was calculated as follows (National Energy Administration, 2010):

$$X_i = \frac{I_i/K_i}{\sum\left(I_i/K_i\right)} \times 100 \quad (1)$$

where i represents the identified mineral, X_i is the proportion of the mineral, I_i is the intensity of the peak of the mineral, calculated by integration of the peak area, and K_i is the reference intensity ratio of the i mineral, with Al_2O_3 used as the known standard for K_i quantification. Please see National Energy Administration (2010) for details about the K_i standard.

2.2.2. Clay fractions

Approximately 50 g of fine powder obtained from each bulk sample were evenly dispersed into 600 mL of distilled water in a beaker. 100 mL of 1% sodium hexametaphosphate solution was added to assist with flocculation. The clay suspension was transferred into another beaker if there was no particle settling observed for about an hour. This suspended fraction was processed by another settling step for 8 h at room temperature (20 °C) (National Energy Administration, 2010), in order to separate the clay fraction (<2 μm) from the solution. The clay fraction was pipetted onto a glass slide and allowed to air dry. After the air-dried clay slide (N-slide) was analysed by XRD as above, it was soaked in an ethylene glycol atmosphere at 60 °C for 8 h in a desiccator. The saturation process causes clay minerals to swell, enabling determination of the presence of expandable clays such as smectite or smectite-bearing minerals (Svensson and Hansen, 2010) in the ethylene-glycol expanded clay slides (E-slide).

The temperature used in the heat treatment process of the E-slide for further better identifying clay minerals was modified based on both testing and reference with USGS OFR01-041 (Poppe et al., 2001) and the SY/T 5163-2018 Standard (National Energy Administration, 2010). Sample X2 was used in an experiment to find the optimal heating temperature for the sample-set (Fig. 3).

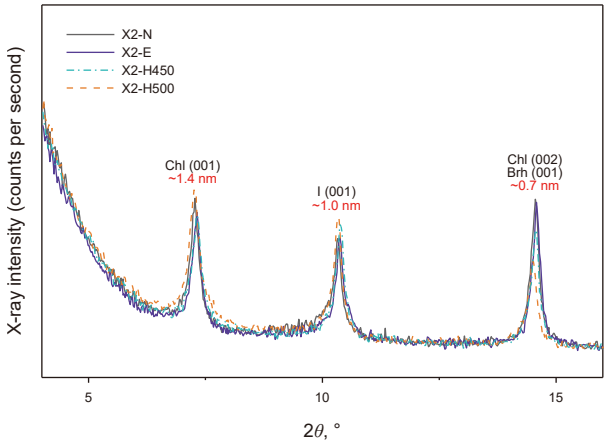

Fig. 3. A snapshot of clay data from the testing process on sample X2. X2-N is the air-dried slide, X2-E is the ethylene-glycol treated slide, X2-H450 is the heated slide made from the X2-E slide that was heated to 450 °C for 2 h, X2-H500 is the heated slide made from the X2-H450 slide that was heated to 500 °C for 2 h. C (001) is the $d_{(001)}$ peak of chlorite, I (001) is the d_{001} peak of illite, C (002) is the d_{002} peak of chlorite, Brh (001) is the $d_{(001)}$ peak of berthierine. ~1.4 nm is the *d*-spacing of C (001), ~1.0 nm is the *d*-spacing of I (001), and ~0.7 nm is the *d*-spacing of C (002) and/or Brh (001).

An increase in intensity occurred for the illite peak (001) in 1.0 nm for both 450 and 500 °C (Fig. 3), potentially indicating transformation of smectite to illite after the heat treatment (Uruowhe, 2021), or perhaps to mixed-layer illite-smectite (I/S). Using a temperature of 500 °C enables the intensity of the dominant chlorite peak ($d_{(001)}$) to increase in the peak at 1.4 nm, which is one of the reflected *d*-spacings for chlorite (Poppe et al., 2001). There was a collapse of the chlorite $d_{(002)}$ (i.e., Chl (002)) peak at 0.7 nm at 450 °C (Worden et al., 2020), but this was more marked at 500 °C (Fig. 3), suggesting that destruction of chlorite was best monitored by heating at 500 °C for 2 h (Poppe et al., 2001), so this heating temperature was adopted for the sample-set (heating slide = H-slide).

All three clay fraction slides were analysed on the Aeris XRD instrument. The radiation intensity in both the incident beam path and the diffracted beam path were adjusted to 0.02, assembled with a divergence slit of 0.125° and a fixed mask of 13 mm. A goniometer scan was set at an angular range of 4°–36°. The scan was performed using a voltage of 40 kV and a current of 15 mA in high resolution mode.

The identification of clay mineral types was conducted on the XRD data of the N-, E- and H-slides using HighScore Plus. The appearance of chlorite can be confirmed by the presence of $d_{(001)}$ and $d_{(002)}$ peaks in the N- and E-slides, with a decrease of intensity of the $d_{(002)}$ peak in the H-slide (Fig. 4(b); Poppe et al., 2001; National Energy Administration, 2010). The $d_{(001)}$ peak of illite consistently existed in the N-, E-, and H-slides (Fig. 4(b)), but with a different intensity on the H-slide when there was a coeluting peak of I/S. The target peak of 0.1–1.54 nm *d*-spacing on the N-slide migrates to larger angles and accumulates as a 1.0 nm *d*-spacing peak on the H-slide, resulting in an increase in the intensity of the 1.0 nm *d*-spacing peak at just above 10° (Fig. 4(b); Poppe et al., 2001; National Energy Administration, 2010). There was no peak with a *d*-spacing of 0.358 nm targeted by HighScore Plus either on the N- or E-slides, suggesting a minor or zero contribution of kaolinite to the clay fraction (Fig. 4(a)). A peak with a *d*-spacing of 1.7 nm was only determined in the X7 sample. This sample does not contain Chl, I, or I/S peaks on the N-slide spectrum (Fig. 4(a)), and the smectite peak disappeared during heating (Fig. 4(c)). The contribution of each identified clay minerals was calculated by the following group of equations (National Energy Administration, 2010):

$$\mathrm{K+Chl} = \frac{\mathrm{I_{0.7nm}(N)}/1.5}{\frac{\mathrm{I_{0.7nm}(N)}}{1.5} + \mathrm{I_{1.0nm}(H)}} \times 100 \quad (2\text{-}1)$$

$$\mathrm{K} = \frac{h_{0.358\mathrm{nm}}(\mathrm{E})}{h_{0.358\mathrm{nm}}(\mathrm{E}) + h_{0.353\mathrm{nm}}(\mathrm{E})} \times (\mathrm{K+Chl}) \quad (2\text{-}2)$$

$$\mathrm{Chl} = (\mathrm{K+Chl}) - \mathrm{K} \quad (2\text{-}3)$$

$$\mathrm{S} = \frac{\mathrm{I_{1.7nm}(E)}/4}{\mathrm{I_{1.0nm}(H)}} \times [100 - (\mathrm{K+Chl})] \quad (2\text{-}4)$$

$$\mathrm{I} = \frac{\mathrm{I_{1.0nm}(E)} \times \left[\frac{h_{0.7\mathrm{nm}}(\mathrm{N})}{h_{0.7\mathrm{nm}}(\mathrm{E})}\right]}{\mathrm{I_{1.0nm}(H)}} \times [100 - (\mathrm{K+Chl})] \quad (2\text{-}5)$$

$$\mathrm{I/S} = 100 - (\mathrm{S+I+K+Chl}) \quad (2\text{-}6)$$

where K is kaolinite, Chl is chlorite, S is smectite, I is illite; $I_{0.7nm}(N)$ is the intensity of the peak with 0.7 nm *d*-spacing on the N-slide, $I_{1.0nm}(H)$ is the intensity of the peak with 1.0 nm *d*-spacing on the H-slide, $h_{0.353nm}(E)$ is the height of the 0.353 nm *d*-spacing peak on

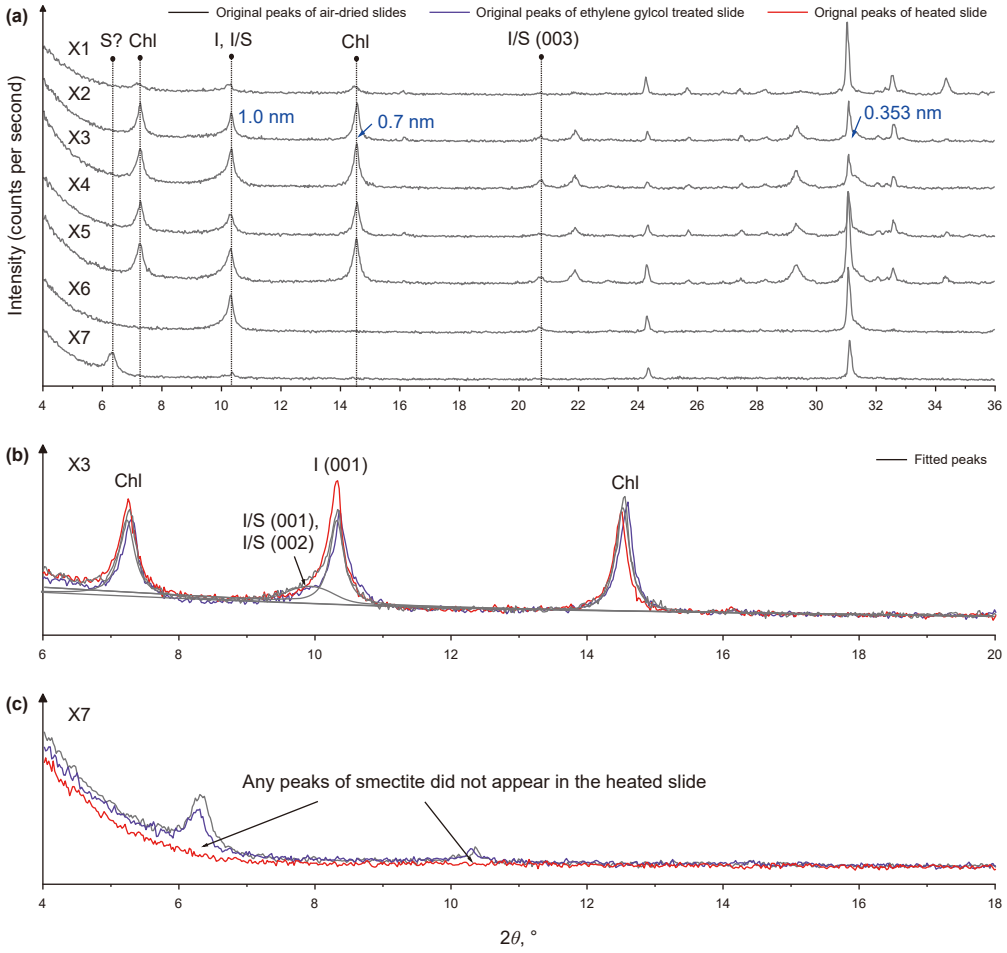

Fig. 4. Identification of clay minerals in the clay fractions of samples X1 to X7 by X-ray diffraction. **(a)** Whole scan results of air-dried slides (N-slide). The blue numbers (1.0 nm, 0.7 nm, and 0.353 nm) are the *d*-spacing values of each peak. **(b)** Peak separation of illite and I/S by symmetric Gauss-Lorentz peak fitting for sample X3. **(c)** Smectite peak identification in sample X7. Chl is chlorite, I is illite, I/S is mixed-layer illite-smectite, S is smectite.

the E-slide, $h_{0.358nm}$(E) is the height of the 0.358 nm *d*-spacing peak on the E-slide, $I_{1.7nm}$(E) is the intensity of the 1.7 nm *d*-spacing peak of smectite on the E-slide, $I_{1.0nm}$(E) is the intensity of the 1.0 nm *d*-spacing peak on the E-slide, and $h_{0.7nm}$(N) is the height of the 0.7 nm *d*-spacing peak on the N-slide. The peaks with *d*-spacing of 0.7, 1.0, 0.353 nm are labelled in blue on Fig. 4(a). All the intensity values were collected from peak integrated areas on the processed spectra in HighScore Plus software.

Peak fitting was used to deconvolute the coeluting I(001), I/S(001), and I/S(002) peaks. A symmetrical peak is expected in the absence of I/S peaks at a *d*-spacing of 1.0 nm, indicating that the actual presence of I(001) in the coeluted peak should have a symmetrical form (National Energy Administration, 2010). A symmetric Gauss-Lorentz function was employed for peak fitting with a fixed peak height, corresponding to the height of *d*-spacing = 1.0 nm on the E-slide. The right side of the fitted peak should overlap with the initial peak on the N-slide, so the I(001) peak was isolated (Fig. 4(b)).

2.3. Scanning electron microscopy

Four samples (Table 1) were analysed by SEM using a Zeiss Sigma 300 instrument in order to obtain information about the spatial relationships between OM and minerals. The thin section samples were polished by an argon ion before SEM analysis. The electron high tension was set at 10 kV, with a working distance of 5–10 mm. A backscattered electron detector was used to ascertain the morphology and content of the minerals. The shape of each mineral was differentiated by contrasting colours, generated by varying intensities of backscattered electrons, resulting in brighter areas associated with heavier elements and darker areas linked to lighter elements. The spatial interaction between OM and minerals was thereby readily studied.

3. Results

3.1. Organic contamination

Both the exterior and interior pieces of the core samples were analysed by GC-MS along with blank samples. The *m/z* 73 mass chromatograms showed a high content of siloxane contamination in the EOM scan of the exterior parts, whereas there were few siloxane peaks in the interior parts. Therefore, the outside surfaces of the cores were contaminated by plastic or water contamination, but this was negligible on the inside. No contaminant or target analyte peaks were observed in either the rotary evaporator-blanks or the sand-blanks, suggesting that no contamination occurred during the laboratory preparation process. Analysis of the aromatic and aliphatic fractions from the interior part of the samples revealed an absence of peaks due to contamination, for

example siloxane or phthalates in *m/z* 73 and *m/z* 149 mass chromatograms. This indicates that any potential minor contamination in the interior part was successfully removed during the fractionation process.

3.2. Polycyclic aromatic hydrocarbons

3.2.1. General distribution of polycyclic aromatic hydrocarbons

The seven samples mainly contain sixteen types of PAHs and their alkyl substituents (Fig. 5). Naphthalene, phenanthrene, pyrene and their alkyl substituents dominate the distribution of PAHs (Figs. 5(a) and 6(a)). Many alkylated substituents of naphthalene, biphenyl, phenanthrene, and dibenzothiophene were identified (Fig. 5(b)–5(j)). The proportion of naphthalene and alkylnaphthalenes ranges from 7% to 66% (average = 41%), the proportion of phenanthrene and alkylphenanthrenes ranges from 15% to 47% (average = 27%), and the proportion of pyrene and alkylpyrenes ranges from 8% to 32% (average = 19%; Fig. 6(a)). There are generally similar proportions of naphthalene and alkylnaphthalenes in the samples, except for sample X6 (Fig. 6(c)). The sum of the alkylnaphthalenes predominate over the proportion of alkylbiphenyls, alkylphenanthrenes, and alkyldibenzothiophenes and averages 68%, except for sample X6 (Fig. 6(c)). Alkylphenanthrenes range from 13% to 30% (except for sample X6), and surpass the amounts of alkylbiphenyls and alkyldibenzothiophenes (Fig. 6(c)). These PAHs are generally derived from aromatisation by thermal processes, or partially originate from biological precursors, and may have been produced by methylation, demethylation, and methyl shifts (Alexander et al., 1985; van Aarssen et al., 1999).

The alkylated substituents of naphthalene, including methylnaphthalenes (MN), dimethylnaphthalene (DMNs), trimethylnaphthalenes (TMN), tetramethylnaphthalenes (TeMN), and pentamethylnaphthalenes (PMN), were identified in the aromatic fractions (Fig. 5(b)–5(e)). The proportions of N and MNs in sample X6 are less than for the other samples (Fig. 6(b)). C_2 alkylnaphthalenes including the DMNs account for 22% to 55% (average = 38%) of the naphthalene and Σalkylnaphthalenes distribution, and the proportion of MNs averages 22% (Fig. 6(b)). Phenanthrene and its alkylated substituents were identified in all samples (Fig. 5(a), (h), (i)), and have somewhat variable distributions between the samples (Fig. 6(d)). Phenanthrene and methylphenanthrenes (MP) dominate the distribution, and there is a slight trend for an increasing relative proportion of phenanthrene

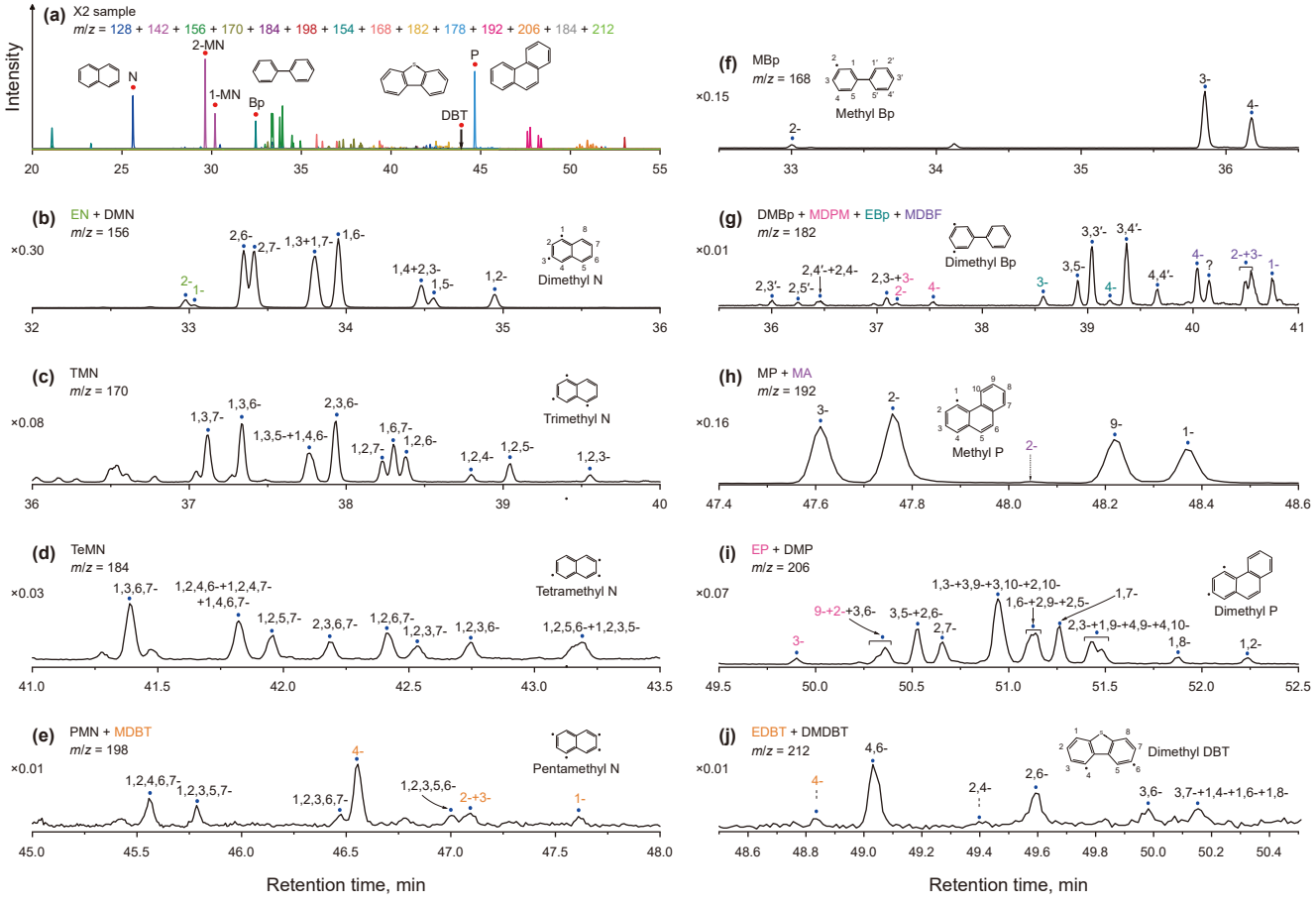

Fig. 5. Partial **(a)** added mass chromatogram (*m/z* = 128 + 142 + 156 + 170 + 184 + 198 +154 + 168 + 182 + 178 + 192 + 206 + 184 + 212) and **(b–j)** separate mass chromatograms for sample X2 showing the identification of alkylated aromatic hydrocarbons. N is naphthalene, MN is methylnaphthalene, EN is ethylnaphthalene, DMN is dimethylnaphthalene, TMN is trimethylnaphthalene, TeMN is tetramethylnaphthalene, PMN is pentamethylnaphthalene, Bp is biphenyl, MBp is methylbiphenyl, DMBp is dimethylbiphenyl, EBp is ethylbiphenyl, MDPM is methyldiphenylmethane, MDBF is methyldibenzofuran, P is phenanthrene, MP is methylphenanthrene, MA is methylanthracene, EP is ethylphenanthrene, DMP is dimethylphenanthrene, EDBT is ethyldibenzothiophene, and DMDBT is dimethyldibenzothiophene. Numbers on the left are the intensity relative to the maximum intensity in (a). The notation with numbers refers to the position of alkylated substituents in the aromatic hydrocarbons.

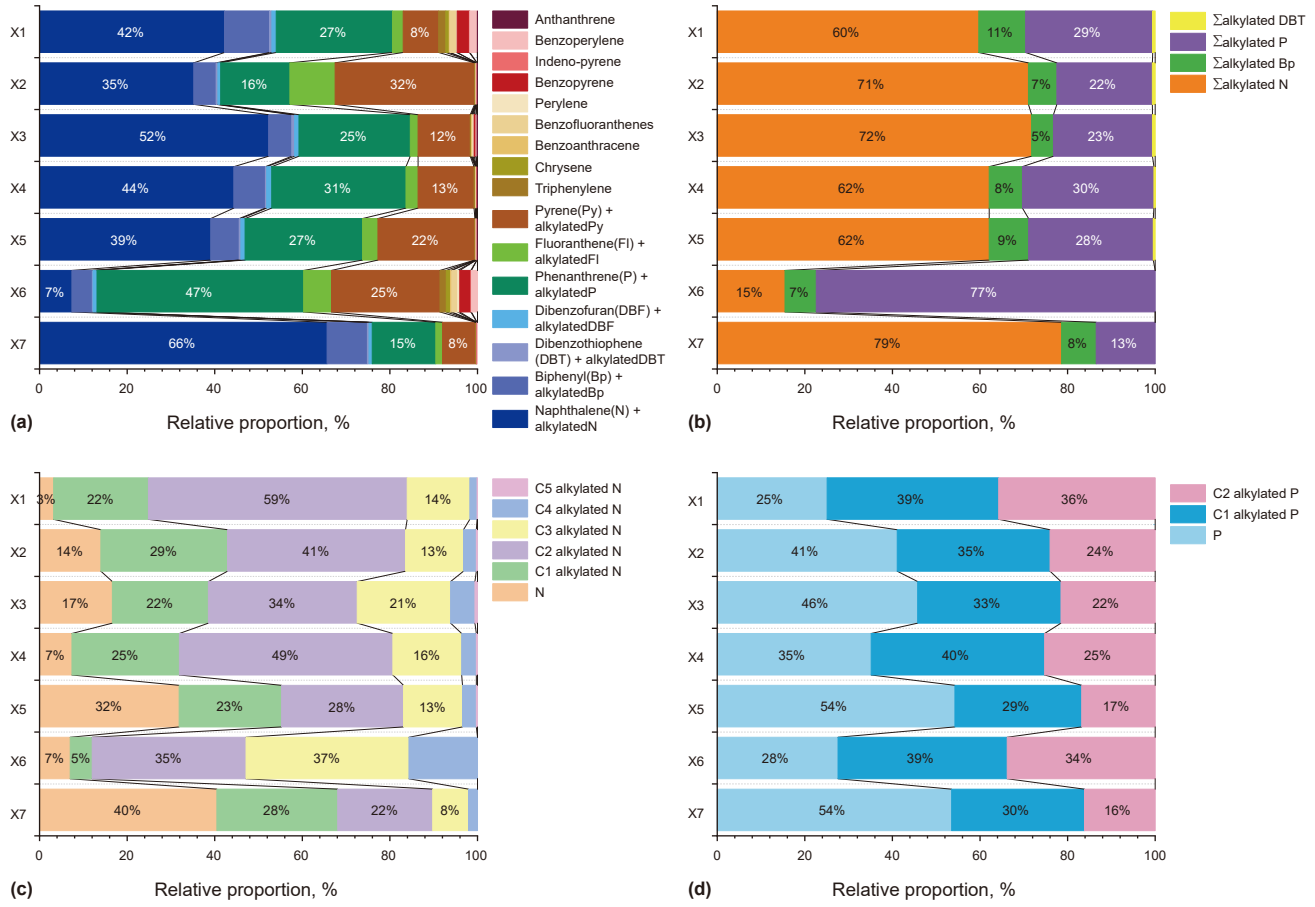

Fig. 6. Bar charts showing the relative proportion of aromatic hydrocarbons in the seven samples: **(a)** all identified aromatic hydrocarbons, **(b)** naphthalene and the alkylnaphthalenes, **(c)** alkylnaphthalenes, alkylbiphenyls, alkylphenanthrenes, and alkyldibenzothiophenes, and **(d)** phenanthrene and the alkylphenanthrenes.

with depth, excluding samples X4 and X6, with a concomitant decrease in C_2 alkylphenanthrenes (Fig. 6(d)). The proportion of methylphenanthrenes is more evenly distributed, and ranges from 29% to 40% of the phenanthrene and Σalkylphenanthrenes distribution (Fig. 6(d)).

Compared to the other samples, sample X6 has different relative proportions of naphthalene and alkylnaphthalenes in the PAHs (Fig. 6(a)), Σalkylnaphthalenes in all alkylated aromatics (N + Bp + P + DBT; Fig. 6(c)), and naphthalene and methylnaphthalenes in naphthalene and Σalkylnaphthalenes (Fig. 6(b)). In particular the distribution of alkylnaphthalenes in sample X6 is abnormal, with greater proportions of C_3, C_4 and C_5 alkylnaphthalenes (Fig. 6(b)). However, the phenanthrene and Σalkylphenanthrenes distribution of sample X6 is similar to the other samples (Fig. 6(d)).

The distribution of N and the alkylnaphthalenes in the EOM of sample X6 could potentially have been affected by biological input, thermochemical sulfate reduction (TSR), the porosity of the lithology, burial heating, interaction with drilling fluids, or evaporation in the laboratory. Sample X6 is located 7 m above sample X7 at the base of the Qiongzhusi Formation (Table 1, Fig. 1(c)), and has a similar lithology and similar inferred biological input as sample X7, so these factors and differential thermal maturity are unlikely to have caused the anomalous alkylnaphthalene distribution in samples X6. Under anaerobic conditions, TSR can be induced by sulfur-reducing bacteria in a marine system (Coates et al., 1996; Lavik et al., 2008). Hydrocarbons, including PAHs, can act as electron donors during TSR (Coates et al., 1996; Guo et al., 2022). The unstable lighter PAHs, for example N and alkylnaphthalenes, can be early targeted compounds during TSR, with sufficient free sulfide ions being generated from sulfate to influence diagenesis (Machel, 2001; Liang et al., 2024). Sediments influenced by TSR typically contain greater amounts of sulfur-bearing minerals (e.g., pyrite; Liang et al., 2024). If the depletion of N and alkylnaphthalenes in sample X6 was due to TSR, it would be expected to contain more pyrite than the other samples, but the XRD data shows that this is not the case (Fig. 7). Metallic chemical drilling fluids are potentially able to destroy aromatic rings, with the appearance of metal-carbon double bonds (Hutskalova and Sparr, 2024). One-ring aromatic compounds, such as benzene, would be first targeted by this process, and would be depleted relative to PAHs, rather than alkylated biphenyls or dibenzothiophenes (Hutskalova and Sparr, 2024). It is highly unlikely that metal-carbon double bond generation could have occurred during the short exposure of the rocks to the water-based drilling muds.

Partial evaporation of N and alkylnaphthalenes caused by excessive nitrogen blow-down in the laboratory is the simplest and most likely reason for the abnormal distribution of alkylnaphthalenes in sample X6 (Ahmed and George, 2004). Accordingly, care has to be taken with interpretation of the alkylnaphthalene ratios in sample X6.

3.2.2. *Isomer distribution of alkylated naphthalenes, phenanthrenes, biphenyls, and dibenzothiophenes*

The position and amount of alkylation in PAHs varies due to methylation, demethylation, and methyl shifts that are induced by

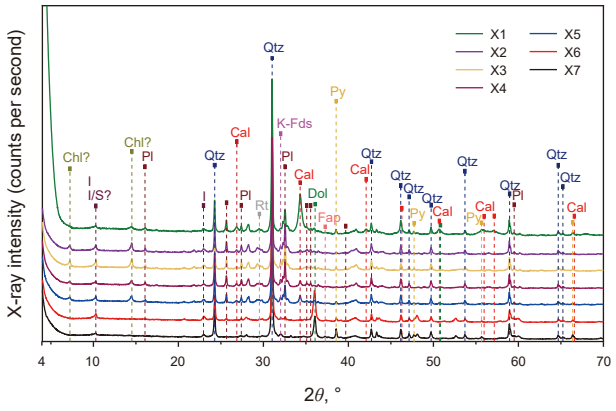

Fig. 7. Identification of minerals from the X-ray diffraction data of the bulk samples X1 to X7. Qtz is quartz, Pl is plagioclase, K-Fds is K-feldspar, Cal is calcite, Dol is dolomite, Py is pyrite, Chl is chlorite, I is illite, I/S is mixed-layer illite-smectite, Rt is rutile, and Fap is fluorapatite.

thermal and chemical catalysis (Alexander et al., 1985; van Aarssen et al., 1999), thus shedding light on the interpretation of burial and thermal alteration of sedimentary rocks. 2-Methylnaphthalene has greater thermal stability compared to 1-methylnaphthalene, and the proportion of 2-methylnaphthalene in the Σmethylnaphthalenes ranges from 60.9% to 71.2% (average = 67.3%; Fig. 8(a)). In the C_2 alkylnaphthalenes, no 1,8-DMN was detected in the samples (Fig. 5(b)). This isomer is $\alpha\alpha$-substituted and is rarely present in mature rocks due to its instability, and therefore significant thermal degradation (Alexander et al., 1985). The proportion of 1,2-DMN is quite variable between the samples, whereas 1,5-DMN has a more uniform distribution (Fig. 8(b); Table 2). There is a relatively high proportion of 2,6-DMN and 2,7-DMN in all samples, both of which are $\beta\beta$-substituted isomers and have high thermal stability. The distribution of C_2 alkylnaphthalenes in the samples is mostly comparable, with the exception of samples X1, X2, and X4, which have slightly elevated proportions of 1,6-DMN (Fig. 8(b)).

In the C_3 alkylnaphthalenes, the resistance of 2,3,6-TMN to thermal alteration is high, and is followed by 1,3,6-TMN and 1,3,7-TMN (Alexander et al., 1985; Radke et al., 1986). Therefore, these compounds are the main peaks in the TMN isomer distribution of the samples (Fig. 8(c)). The minor proportion of 1,2,5-TMN compared to 1,3,6-TMN in the distribution could either have been caused by OM originating from a marine environment (Asahina and Suzuki, 2018), or more likely is a result of high thermal maturity (van Aarssen et al., 1999) (Fig. 8(c)). It has been suggested that 1,3,6,7-TeMN is more abundant in thermally-mature rocks relative to the other C_4 alkylnaphthalenes due to its resistance to thermal alteration (van Aarssen et al., 1999), and it predominates in the distribution of C_4 alkylnaphthalenes (Fig. 8(d)). However, the relative proportion of 1,3,6,7-TeMN is noticeably less in samples X6 and X7 sample compared to the other samples. In addition to 1,3,6,7-TeMN (an $\alpha\beta\beta\beta$-substituted isomer) and 2,3,6,7-TeMN (a $\beta\beta\beta\beta$-substituted isomer) (van Aarssen et al., 1999; van Duin et al., 1997), the other alkylated substituents of naphthalene in oils and mature rocks predominantly consist of β-substituted rather than α-substituted methyls (van Aarssen et al., 1999). This suggests that the alkylnaphthalene isomer distributions in the early Cambrian samples are reliable (Fig. 8(a)–8(d)), and are useful as thermal maturation indicators at high maturities.

The β-substituted 2-methylphenanthrene is the most abundant of the methylphenanthrenes in all samples, ranging from 30.6% to 36.9% of Σmethylphenanthrenes (average = 33.5%; Fig. 8(e)). 1-Methylphenanthrene, which has an α-substituted methyl group, is present in the lowest proportion (16.6% to 18.7%; Fig. 8(e)). The largest proportion of C_2 alkylphenanthrenes is peak f4, which is due to co-eluting 1,3- + 3,9- + 2,10- + 3,10-dimethylphenanthrene (DMP) (Fig. 5(i) and 8(f)). The samples have similar relative proportions of C_2 alkylphenanthrenes.

The dominant methylbiphenyl is 3-methylbiphenyl (MBp), which has a relative proportion of 57.2% to 64.8% of Σmethylbiphenyls (average = 60.1%; Fig. 8(g)). 2-MBp is an α-substituted isomer, and has the lowest fraction in the distribution (Fig. 8(g)). 3,3′-dimethylbiphenyl (DMBp) and 3,4′-DMBp both have $\beta\beta$-substituted methyl groups, and are the most dominant isomers of the C_2 alkylbiphenyls (Fig. 5(g) and 8(h)). Comparably, the isomer 2,5′-DMBp has two α-substituted methyl groups, and forms the lowest proportion of C_2 alkylbiphenyls (1.6% to 4.6%; Fig. 8(h)). The samples have generally similar relative proportions of C_1 and C_2 alkylbiphenyls.

Methyldibenzothiophenes (MDBT) and dimethyldibenzothiophenes (DMDBT) were hardly detected in samples X6 and X7, probably due to the sulfur equilibrium between organic and inorganic systems in euxinic sedimentary conditions (Abubakar et al., 2022). 1-MDBT has the lowest proportion of the distribution in the other samples, while 4-MDBT varies in proportions >50% (Fig. 8(i)). DMDBTs have an inconsistent and variable distribution in the samples (Fig. 8(j)). Generally, 4,6-DMDBT has the largest proportion of the C_2 dibenzothiophenes, followed by the co-eluting peak due to 3,7- + 1,4- + 1,6- + 1,8-DMDBT (Fig. 8(j)).

3.2.3. Thermal maturity ratios based on alkylated naphthalenes, phenanthrenes, biphenyls, and dibenzothiophenes

Table 3 lists the numerous alkylated aromatic ratios that vary with thermal maturity for the seven samples, along with ratio definitions. The methylnaphthalene ratio (MNR) ranges from 1.6 to 2.5 (average = 2.1). The dimethylnaphthalene ratio (DNR-1) has significant variation (5.1–12.5), with an average of 8.4. Sample X1 has the highest DNR-1, while sample X3 has the lowest. One trimethylnaphthalene ratio (TNR-1) has values scattered from 1.1 to 1.9 (average = 1.5). The TNR-2 varies less than TNR-1, from 0.91 to 1.32 (average = 1.1). Another trimethylnaphthalene ratio (TMNr) has a narrow range (0.63–0.80; average = 0.71). One tetramethylnaphthalene ratio (TeMNR-1) has a range of 0.95–1.75 (average = 1.16). Another tetramethylnaphthalene ratio (TeMNr) has a narrower range (0.57–0.70; average = 0.65). The lowest values for these maturity-dependent alkylated naphthalene ratios are generally for sample X7, with the exceptions of MNR and DNR-1. The highest values are mostly for sample X1, apart from MNR, TNR-1, and TNR-2.

Four thermal-dependent alkylated phenanthrene ratios are widely used, including the methylphenanthrene index (MPI), the methylphenanthrene distribution fraction (MPDF), a methylphenanthrene ratio (MPR), and the dimethylphenanthrene ratio (DMPR) (Table 3). The values of MPI and MPR in the samples have a greater range compared to MPDF and DMPR. MPI varies from 0.59 to 1.1 (average = 0.85). The MPR values range from 1.7 to 2.2 (average = 1.9). Both the MPI and MPR are lowest in sample X7. The MPDF varies from 0.58 to 0.65 (average = 0.60). The DMPR range from 0.35 to 0.48 (average = 0.39). Both the MPDF and DMPR are highest in sample X5.

Three thermal-dependent alkylbiphenyl ratios are used in this study (Table 3). The methylbiphenyl ratio (MBpR) of the samples varies from 0.28 to 1.12 (average = 0.63). Both the dimethylbiphenyl ratios (DMBpR-x and DMBpR-y) have a wider variation in their distribution than the MBpR. The DMBpR-x varies from 3.2 to 8.0 (average = 4.6). The DMBpR-y varies from 6.4 to 15

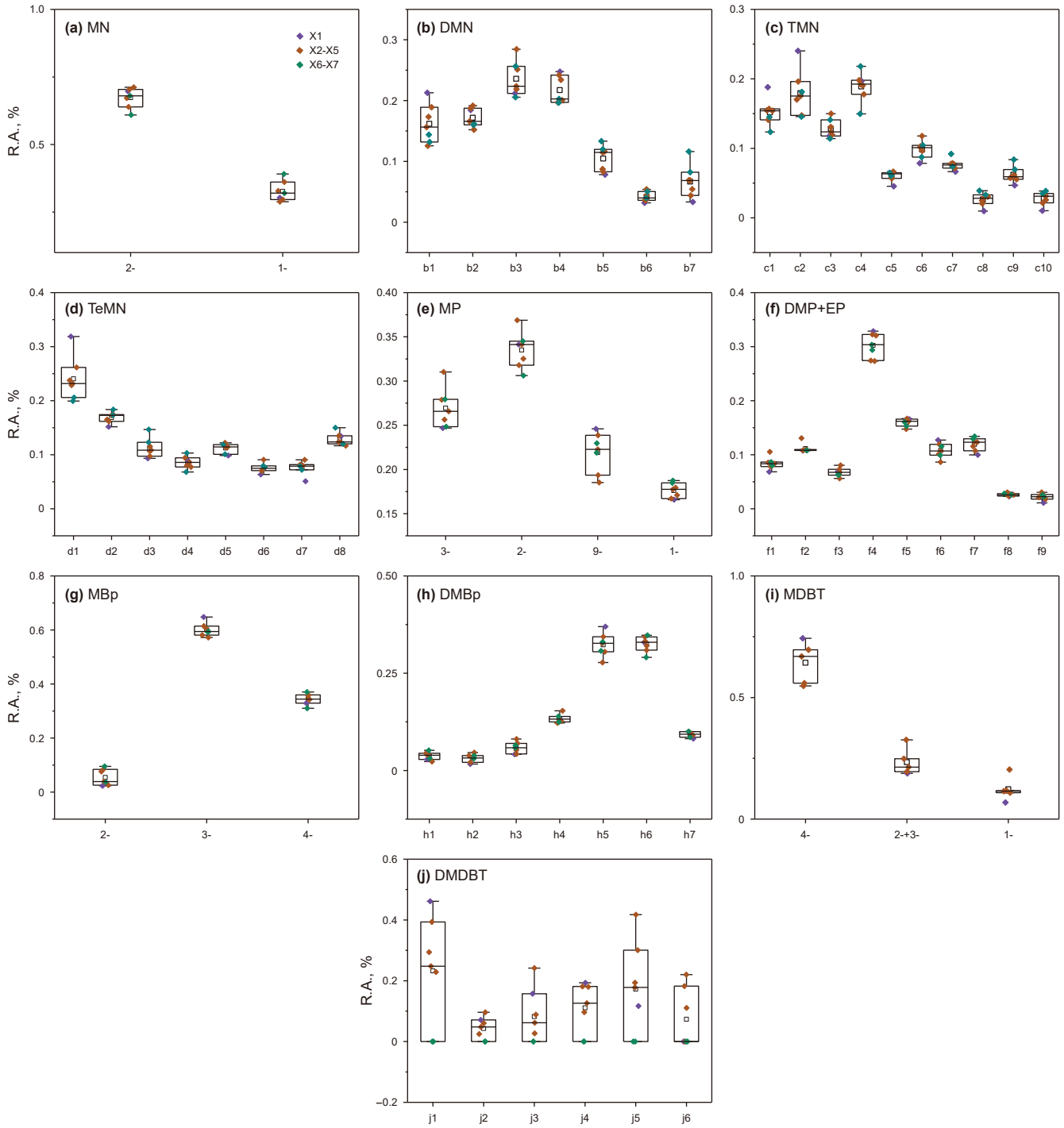

Fig. 8. Isomer distribution of **(a–d)** alkylnaphthalenes, **(e–f)** alkylphenanthrenes, **(g–h)** alkylbiphenyls, and **(i–j)** alkyldibenzothiophenes. The sample legend in (a) refers to all panels. MN is methylnaphthalene, DMN is dimethylnaphthalene, TMN is trimethylnaphthalene, TeMN is tetramethylnaphthalene, MP is methylphenanthrene, DMP is dimethylphenanthrene, EP is ethylphenanthrene, MBp is methylbiphenyl, DMBp is dimethylbiphenyl, MDBT is methyldibenzothiophene, and DMDBT is dimethyldibenzothiophene. R.A. is the abbreviation of Relative Abundance, The labels of the alkylated isomers in each graph are listed in Table 2.

(average = 9.5). The MBpR and DMBpR-x are highest in sample X1, and the MBpR and DMBpR-y are lowest in sample X7.

The five samples in which alkyldibenzothiophene ratios were measured have a methyldibenzothiophene ratio (MDR) of 2.7–10.9 (average = 6.1). The distribution of the dimethyldibenzothiophene ratio (DMDR) has a narrower range (1.0–1.8; average = 1.3). The MDR and DMDR are lowest in sample X3.

The values of these maturity-dependent aromatic ratios have inconsistent variations, both in the extremes for the samples, and the trends between samples. This suggests that these thermal maturity ratios might be partly affected by other factors.

3.3. Mineralogy of samples

3.3.1. Distribution of minerals

Eight minerals were identified by the XRD scan results in the bulk samples, together with some clay minerals (Fig. 7). The proportion of quartz roughly increases with depth, ranging from 36.8%

Table 2
Labels of the alkylaromatic isomers for panels b, c, d, f, h, and j in Figure 6.

Dimethylnaphthalenes		Trimethylnaphthalenes		Tetramethylnaphthalenes		Dimethylphenanthrenes		Dimethylbiphenyls		Dimethyldibenzothiophenes	
b1	2,6-	c1	1,3,7-	d1	1,3,6,7-	f1	9- + 2-EP + 3,6-	h1	2,3'-	j1	4,6-
b2	2,7-	c2	1,3,6-	d2	1,2,4,6- + 1,2,4,7- + 1,4,6,7-	f2	3,5- + 2,6-	h2	2,5-	j2	2,4-
b3	1,3- + 1,7-	c3	1,3,5- + 1,4,6-	d3	1,2,5,7-	f3	2,7-	h3	2,4'- + 2,4-	j3	2,6-
b4	1,6-	c4	2,3,6-	d4	2,3,6,7-	f4	1,3- + 3,9- + 2,10- + 3,10-	h4	3,5-	j4	3,6-
b5	1,4- + 2,3-	c5	1,2,7-	d5	1,2,6,7-	f5	1,6- + 2,9- + 2,5-	h5	3,3'-	j5	3,7- + 1,4- + 1,6- + 1,8-
b6	1,5-	c6	1,6,7-	d6	1,2,3,7-	f6	1,7-	h6	3,4'-	j6	1,3- + 1,9- + 1,2-
b7	1,2-	c7	1,2,6-	d7	1,2,3,6-	f7	2,3- + 1,9- + 4,9- + 4,10-	h7	4,4'-		
		c8	1,2,4-	d8	1,2,5,6- + 1,2,3,5-	f8	1,8-				
		c9	1,2,5-			f9	1,2-				
		c10	1,2,3-								

in the shallowest sample (X1) to 59.7% in the deepest samples (X7; Table 4). K-feldspar is more abundant in samples X2–X5, with an average of 6.1%. Plagioclase has a comparable distribution to K-feldspar, with the largest proportion in samples X2–X5 (average = 25.4%), followed by sample X1 (average = 16.3%). Plagioclase is present in a low proportion in samples X6 and X7 (average = 1.9%). Calcite is much more abundant in sample X1 (average = 33.2%) compared to the other samples. Samples X3, X6 and X7 hardly contain any calcite, and samples X2, X4, and X5 have an average proportion of 4.3% (Table 4). Conversely, there are significant amounts of dolomite in samples X6 and X7 (average = 25.3%), whereas very little dolomite was identified in samples X1–X5 (Fig. 7). Fluorapatite has a similar distribution as K-feldspar, with the lowest proportion in samples X2, X3, X4 and X5 (average = 0.5%), and larger proportions in samples X6 and X7 (average = 3.7). Total clays compose 8.7% of the minerals in sample X1, and is higher (average = 15.9%) in samples X2–X5. Total clays average 9.4% in samples X6 and X7 (Table 4). Based on the XRD results on the bulk samples, three mineralogy types were identified in the sample sequence. These are termed mineralogical unit 1 (sample X1), unit 2 (samples X2–X5), and unit 3 (samples X6–X7; Table 4).

The presence of clay minerals in the samples was confirmed using XRD analysis of the clay fractions (Fig. 4(a)). Three types of clay minerals were positively identified: chlorite, illite, and I/S. The peaks observed in the clay patterns of sample X1 are rather minor, which aligns with the results from the bulk sample analyses (Fig. 7; Table 4). Accordingly, care needs to be taken in interpreting the relative proportions of clay minerals in this sample. The clay fraction of sample X6 has prominent illite and I/S peaks, but chlorite and smectite are absent (Fig. 4(a)). Sample X7 has a single peak of smectite in both the air-dried slide and the ethylene glycol slide (Fig. 4(c)), which potentially could be due to depositional conditions (Han et al., 2022; Xu et al., 2024), or contamination. However, no smectite peak was observed in the heated slide (Fig. 4(c)), which may be due to just a small amount of smectite in the clay fraction being destroyed. The relative proportions of clay minerals in samples X2–X5 were calculated (Table 4). Illite ranges from 36.7% to 55.3% (average = 49.0%). Chlorite ranges from 27.5% to 43.8%, (average = 37.5%). Sample X4 contains the largest proportion of I/S (35.8%), but in the other samples there is <10% I/S.

3.3.2. Illite crystallinity

Illite crystallinity is used to monitor the effects of diagenesis and burial metamorphic processes, due to the known effect of pressure and temperature on the crystallisation of illite, for example during the muscovite to illite reaction (Verdel et al., 2011). Illite crystallinity is assessed by the Kubler index (KI) (Eberl and Velde, 1989; Gharrabi et al., 1998; Warr and Cox, 2016), which is calculated based on the full width at half maximum height of the (001) peak using the gaussian LorenCross function (Eberl and Velde, 1989; Gharrabi et al., 1998). The KI decreases with increasing metamorphic intensity, and samples are classified to be in the prehnite-pumpellyite metamorphic grade if KI is 0.2–0.4, with a maximum temperature of about 200–300 °C (Verdel et al., 2011). The co-eluting peak of illite and I/S was separated based on both the air-dried slide and the ethylene glycol slide (Fig. 4(b)). The KI of samples X1 and X2 is 0.23, while it is higher for samples X3–X5 (average = 0.31; Table 4), suggesting less heating for these samples. Sample X6 has an intermediate KI (0.27).

3.4. Spatial relationships between organic matter and minerals

Four samples with a large variety of both mineralogy and KI were selected for SEM to assess the spatial relationship between

Table 3
Thermal maturity-dependent alkylated aromatic ratios and their definitions.

			Samples						
Maturity-dependent aromatic ratios	Abbrev-iation	Definition	X1	X2	X3	X4	X5	X6	X7
Methylnaphthalene ratio	MNR	2-MN/1-MN	2.3	2.4	1.8	2.5	2.0	1.6	2.1
Dimethylnaphthalene ratio	DNR-1	(2,6- + 2,7-DMN)/1,5-DMN	12.5	10.2	5.1	10.4	7.3	5.8	7.7
Trimethylnaphthalene ratios	TNR-1	2,3,6-TMN/(1,4,6- + 1,3,5-TMN)	1.7	1.5	1.2	1.6	1.7	1.9	1.1
	TNR-2	(2,3,6- + 1,3,7-TMN)/(1,4,6- + 1,3,5- + 1,3,6-TMN)	1.07	1.13	1.07	1.08	1.22	1.32	0.91
	TMNr	1,3,7-TMN/(1,3,7- + 1,2,5-TMN)	0.80	0.73	0.70	0.73	0.73	0.64	0.63
Tetramethylnaphthalene ratios	TeMNR-1	2,3,6,7-TeMN/1,2,3,6-TeMN	1.75	0.95	1.03	1.00	1.15	1.31	0.95
	TeMNr	1,3,6,7-TeMN/(1,3,6,7- + 1,2,5,6- + 1,2,3,5-TeMN)	0.70	0.65	0.66	0.66	0.66	0.63	0.57
Methylphenanthrene index	MPI	[1.5 × (3-MP + 2-MP)]/(P + 9-MP + 1-MP)	1.10	0.80	0.79	0.92	0.65	1.06	0.59
Methylphenanthrene distribution fraction	MPDF	(3-MP + 2-MP)/ΣMPs	0.59	0.60	0.64	0.58	0.65	0.59	0.59
Methylphenanthrene ratio	MPR	2-MP/1-MP	2.1	1.9	1.9	1.8	2.2	1.8	1.7
Dimethylphenanthrene ratio	DMPR	(3,5- + 2,6- + 2,7-DMP)/(1,3- + 3,9- + 2,10- + 3,10- + 1,6- + 2,9- + 2,5-DMP)	0.36	0.42	0.35	0.36	0.48	0.38	0.37
Methylbiphenyl ratio	MBpR	3-MBp/2-MBp	1.12	0.48	0.43	0.96	0.50	0.61	0.28
Dimethylbiphenyl ratios	DMBpR-x	3,5-DMBp/2,5-DMBp	8.0	3.9	3.3	6.3	3.2	4.0	3.7
	DMBpR-y	3,3′-DMBp/2,3′-DMBp	13.0	8.3	7.1	15.0	6.9	9.9	6.4
Methyldibenzothiophene ratio	MDR	4-MDBT/1-MDBT	10.9	4.9	2.7	6.4	5.7	nd	nd
Dimethyldibenzothiophene ratio	DMDR	4,6-DMDBT/(3,6- + 2,6-DMDBT)	1.3	1.1	1.0	1.8	1.1	nd	nd

MNR, DNR-1, MPR, and DMPR are from Radke et al. (1982b); TNR-1 is from Alexander et al. (1985); TNR-2 and MDR are from Radke et al. (1986); TeMNR-1 is from George et al. (1996); TMNr and TeMNr are from van Aarssen et al. (1999); MPI is from Radke et al. (1982a); MPDF is from Kvalheim et al. (1987); MBpR is from Alexander et al. (1986); DMBpR-x and DMBpR-y are from Cumbers et al. (1987); DMDR is from George et al. (2001). nd = not determined.

Table 4
The relative proportions of minerals in the bulk samples, the relative proportions of clay minerals in the clay fractions, and the Kubler Index (KI; illite crystallinity).

	Bulk samples, %									Clay fractions, %			Mixed layer		Illite crystallinity
	Qtz	K-Fds	Pl	Cal	Dol	Py	Fap	Rt	Clay	I	Chl	I/S	I	S	Kubler Index
X1	36.8	1.1	16.5	32.4	0.0	2.5	0.0	2.1	8.5	nd	nd	nd	nd	nd	0.23
X2	38.7	7.0	31.4	2.1	0.6	0.9	0.0	0.8	18.5	49.4	43.8	6.9	95	5	0.23
X3	45.3	6.6	23.2	0.0	1.5	3.1	0.8	1.1	18.4	54.7	36.2	9.1	95	5	0.32
X4	52.7	5.7	25.6	4.3	1.1	0.3	0.5	0.0	9.9	36.7	27.5	35.8	95	5	0.31
X5	47.9	5.0	20.3	6.4	1.3	2.0	0.9	0.0	16.2	55.3	42.5	2.1	95	5	0.31
X6	46.2	2.4	3.6	0.0	28.8	2.6	3.6	0.0	12.7	pr	nd	pr	nd	nd	0.27
X7	59.7	3.7	0.0	0.0	20.1	7.6	3.5	0.0	5.5	nd	nd	nd	nd	nd	nd

Qtz is quartz, K-Fds is K-feldspar, Pl is plagioclase, Cal is calcite, Dol is dolomite, Py is pyrite, Fap is fluorapatite, Rt is rutile, I is illite, Chl is chlorite, I/S is mixed-layer illite-smectite, nd = not determined, and pr = present. The Kubler Index is the illite XRD peak, full width at half maximum height of the (001) peak.

the OM and the clays (Table 1, Fig. 9). Some corrosion pores are present in all samples (Fig. 9(a),(d),(g),(j)). X2-1 and X2-2 are from the upper part of sample X2, and are silty mudstone with a larger proportion of clay than muddy siltstone. The contact relationships between laths of illite and I/S are possible to see when the corrosion pores are magnified (Fig. 9(b),(e)), suggesting that the pores offered a place for diagenetic alteration of the clays. There are two general mechanisms of transformation from smectite to illite during diagenesis (Yuan et al., 2019b; Mills et al., 2023), requiring sufficient thermal heating and the influx of K^+ and H^+ (Mosser-Ruck et al., 2001; Cuadros, 2006; Yuan et al., 2019b; Mills et al., 2023), and are typically accompanied by the release of silica (Mills et al., 2023). In sample X2-1 (depth = 1217.21–1219.18 m), illite and I/S occur in tight contact (Fig. 9(b)). Some illite crystals appear to have nucleated directly on OM surfaces (Fig. 9(c)), in association with altered K-feldspar, which likely supplied K^+ for illitisation. In sample X2-2 (1219.58–1222.12 m), illite fibres extend into a pore filled with OM (Fig. 9(f)). The nearby occurrence of silica suggests concurrent silica and illite precipitation, potentially linked to the illitisation process. However, the mechanism of illite growth into the OM is still unknown.

Sample X3-1 (1225.99–1228.04 m) is a muddy siltstone with generally higher porosity than mudstone, and has pronounced dissolution features in intercrystalline zones of K-feldspar and I/S (Fig. 9(h)), potentially due to post diagenetic alteration (Liu et al., 2017; Yuan et al., 2019b). These intercrystalline domains may have provided pathways for pore waters enriched in K^+ and H^+. Another contact of OM and clays in sample X3-1 (Fig. 9(i)) is associated with very clean-shaped OM in contact with a quartz grain, which is coated by detrital clay silt grains, rather than clays in tight contact with the surface of the OM.

In the deeper X7-1 sample some clays, either smectite or laths of illite, are distributed on the boundary of microcrystalline dolomites (Fig. 9(k) and (l)), indicating that the generation and alteration of smectite may have been involved with dolomite growth (Han et al., 2022), and may have occurred geologically late.

Overall, these petrographic observations consistently demonstrate a tight spatial relationship between OM and illite across different lithologies. Such observations provide the basis for a working hypothesis that the spatial proximity of OM and illite may be linked to simultaneous processes of OM thermal alteration and clay transformation during burial.

4. Discussion

4.1. Variation of organic matter thermal maturity

Aromatic hydrocarbons in early Cambrian sediments in other basins are mostly heavily thermally altered (Awan et al., 2023; Hall, 2012; Qiu et al., 2021), and were involved in oil and gas generation processes (Peng et al., 2020; Tang et al., 2019; Tao et al., 2012). Alkylated PAHs and their distributions have been

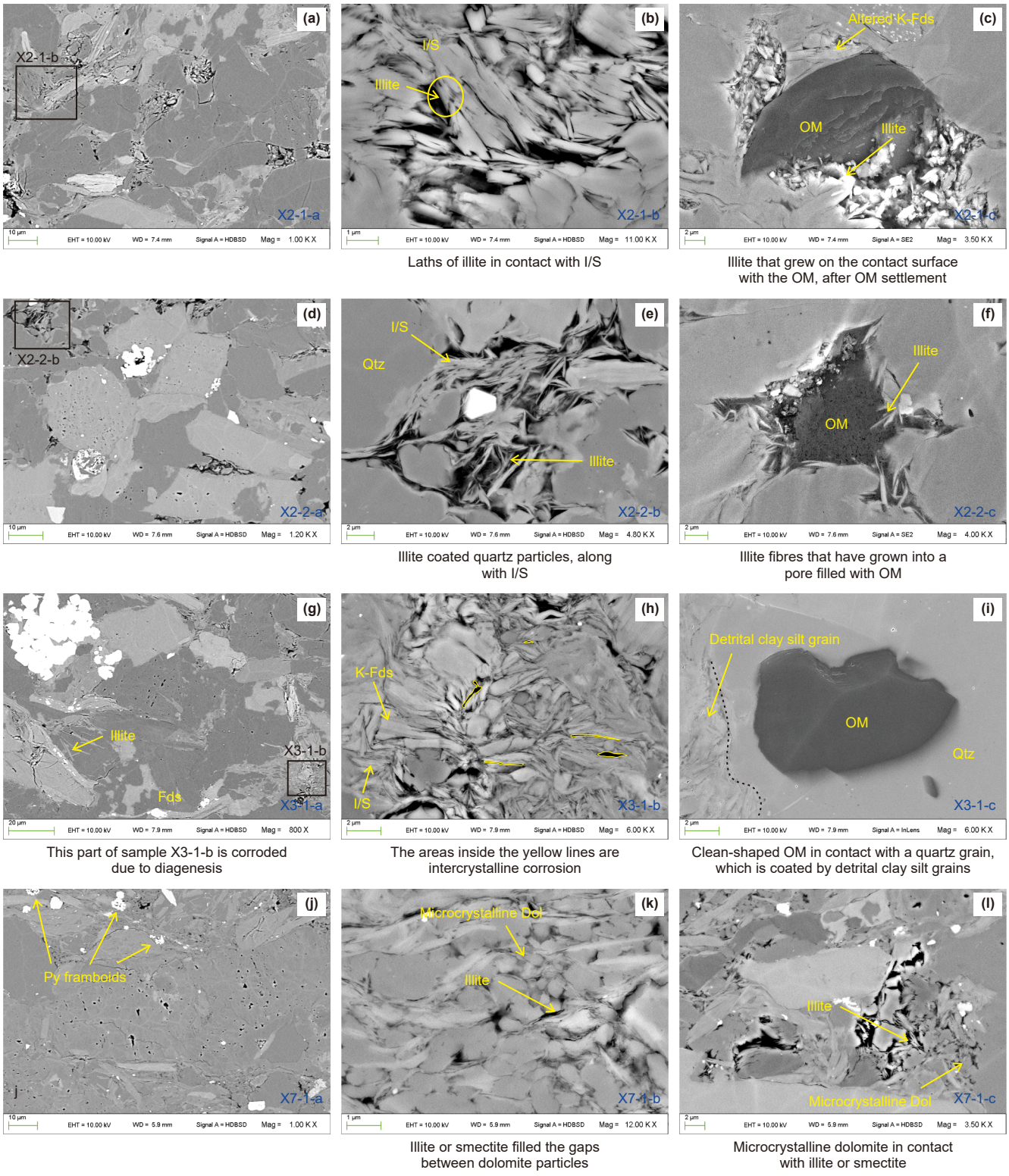

Fig. 9. Scanning electron microscopy images showing the spatial contacts between organic matter (OM) and clays in samples X2-1, X2-2, X3-1, and X7-1. I/S = mixed-layer illite-smectite, Qtz = quartz, K-Fds = K-feldspar, Py = pyrite.

extensively studied in different thermal maturity source rocks (e.g., Asahina and Suzuki, 2018; George and Ahmed, 2002; Radke et al., 1986). The thermal stability of the methylated functional groups associated with PAHs varies, making them suitable as markers of both thermal maturity and oil/gas generation (Alexander et al., 1985, 1986; Budzinski et al., 1993; Mi et al., 2018; Peng et al., 2020). The thermal-dependent aromatic ratios described in Section 3.2.3 were plotted along with data from reference samples of varying thermal maturity from the Meso-proterozoic Velkerri Formation (George and Ahmed, 2002), in

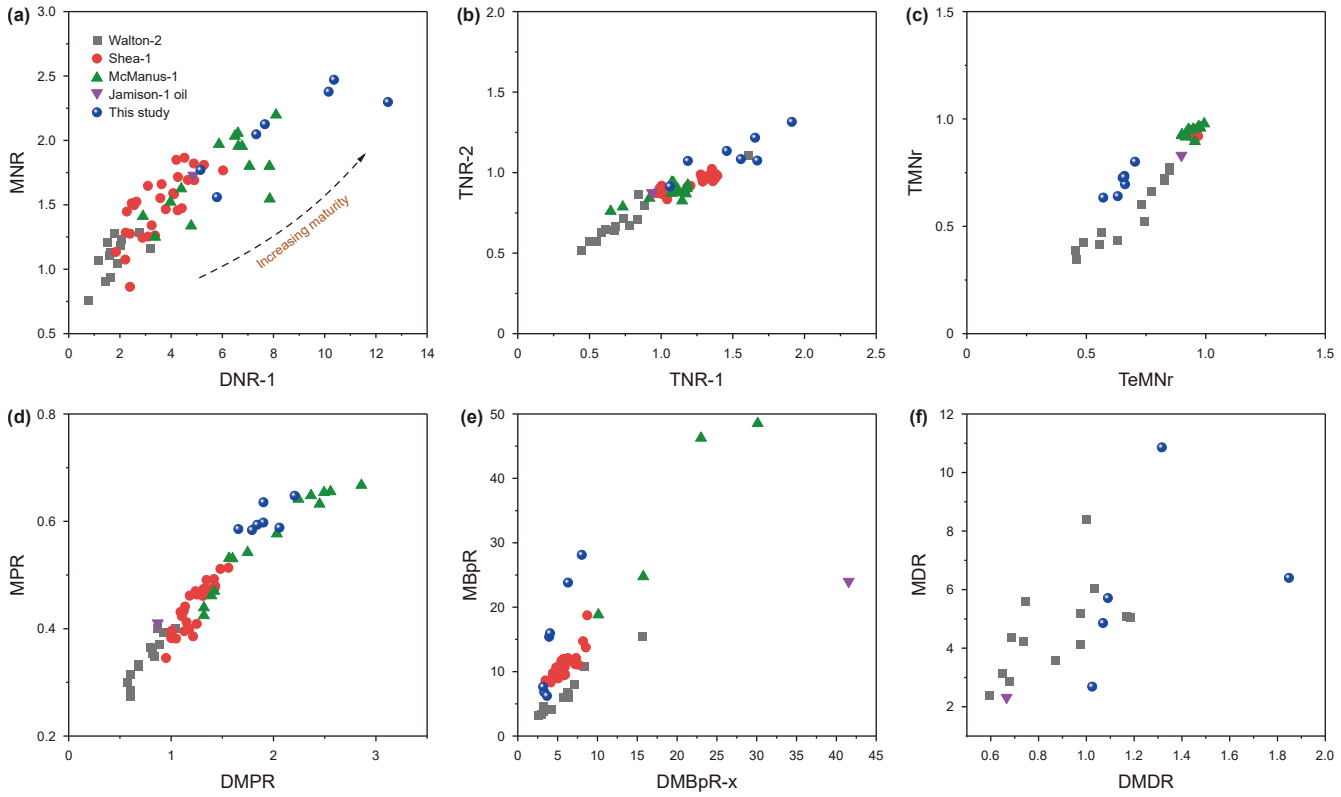

Fig. 10. Cross plots of thermally-dependent aromatic ratios for samples from this study (blue solid balls) compared to a reference set of samples from the Mesoproterozoic Velkerri Formation (George and Ahmed, 2002), which includes samples from the early oil window (Walton-2), the main part of the oil window (Shea-1), and the gas window (McManus-1). **(a)** Methylnaphthalene ratio (MNR) versus dimethylnaphthalene ratio (DNR-1), **(b)** trimethylnaphthalene ratio (TNR-2) versus trimethylnaphthalene ratio (TNR-1), **(c)** trimethylnaphthalene ratio (TMNr) versus tetramethylnaphthalene ratio (TeMNr), **(d)** methylphenanthrene ratio (MPR) versus dimethylphenanthrene ratio (DMPR), **(e)** methylbiphenyl ratio (MBpR) versus dimethylbiphenyl ratio (DMBpR-x), **(f)** methyldibenzothiophene ratio (MDR) versus dimethyldibenzothiophene ratio (DMDR). The ratios are defined in Table 3.

order to determine the thermal maturity level of EOM in the Zhaotong borehole samples (Fig. 10). The Velkerri Formation was used as a reference, because of the lack of published aromatic hydrocarbon data for early Cambrian sediments in the Yangtze Platform. The Velkerri Formation sediments were deposited in the McArthur Basin, in the northern part of Australia (e.g., Noorian et al., 2025), and were evaluated as type I/II organic matter (Warren et al., 1998), which are thus similar to the kerogen in the early Cambrian sediments from the Yangtze Platform (Awan et al., 2020, 2023; Hu et al., 2012). However, considering that the initial alkylated PAHs in the early Cambrian sediments were likely distinct from those in the Precambrian due to different biological components, multiple ratios were used in several cross plots for examining thermal maturity.

The thermal maturity of the reference samples are early oil-window (Walton-2), peak oil window (Shea-1), and gas-window (McManus-1). The cross plots of MNR versus DNR-1 (Fig. 10(a)), TNR-1 versus TNR-2 (Fig. 10(b)), and MPR versus DMPR (Fig. 10(d)) have consistent and positive trends with increasing thermal maturity. Samples in this study mainly plot in the area of the gas window, with similar values as in McManus-1 (Fig. 10(a), (b), (d)). Interestingly, the cross plots of TMNr versus TeMNr (Fig. 10(c)) and MBpR versus DMBpR-x (Fig. 10(e)) give a different result. The studied samples exhibit a close but slightly displaced distribution compared to the early oil-window Walton-2 samples based on TMNr versus TeMNr (Fig. 10(c)), suggesting that the trimethylnaphthalene and tetramethylnaphthalene isomers used in these ratios were less thermally altered than the C_1 and C_2 alkylated naphthalenes, the C_1 alkylphenanthrenes, and indeed other trimethylnaphthalene isomers used in the TNR-1 and TNR-2 parameters (Table 3). There is large variation in the MBpR parameter for the studied samples, although the DMBpR-x varies less (Fig. 10(e)). Samples from the early oil-window (Walton-2) and peak oil window (Shea-1) reference set have little variability for these alkylbiphenyl parameters, whereas there is much greater variation for the gas-window McManus-1, which was attributed to these parameters being only sensitive to higher thermal maturities (George and Ahmed, 2002). However, the anomalous thermal maturity ratios based on some trimethylnaphthalene and tetramethylnaphthalene isomers and alkylbiphenyls suggest the influence of other factors.

The chemical structures of these aromatic hydrocarbons may partly be the key to explaining these anomalies. A relatively high abundance of both 1,2,5-TMN and 1,2,5,6-TeMN is apparent in the distribution of the alkylnaphthalenes (Fig. 10(c)), which is inconsistent with the other data suggesting a gas window thermal maturity. 1,2,5-TMN and 1,2,5,6-TeMN can be the products of plant precursor inputs, such as β-amyrin, cadinenes or cadinols (Püttmann and Villar, 1987; van Aarssen et al., 1999). However, in these early Cambrian sediments it is not possible to have a primary higher plant OM source (Shu, 2008; Sun et al., 2020), unless there was a secondary input of OM migrated from younger sediments (e.g., Late Permian; Manda et al., 2023). However, there is no tectonic evidence that supports a phase of migration of younger OM

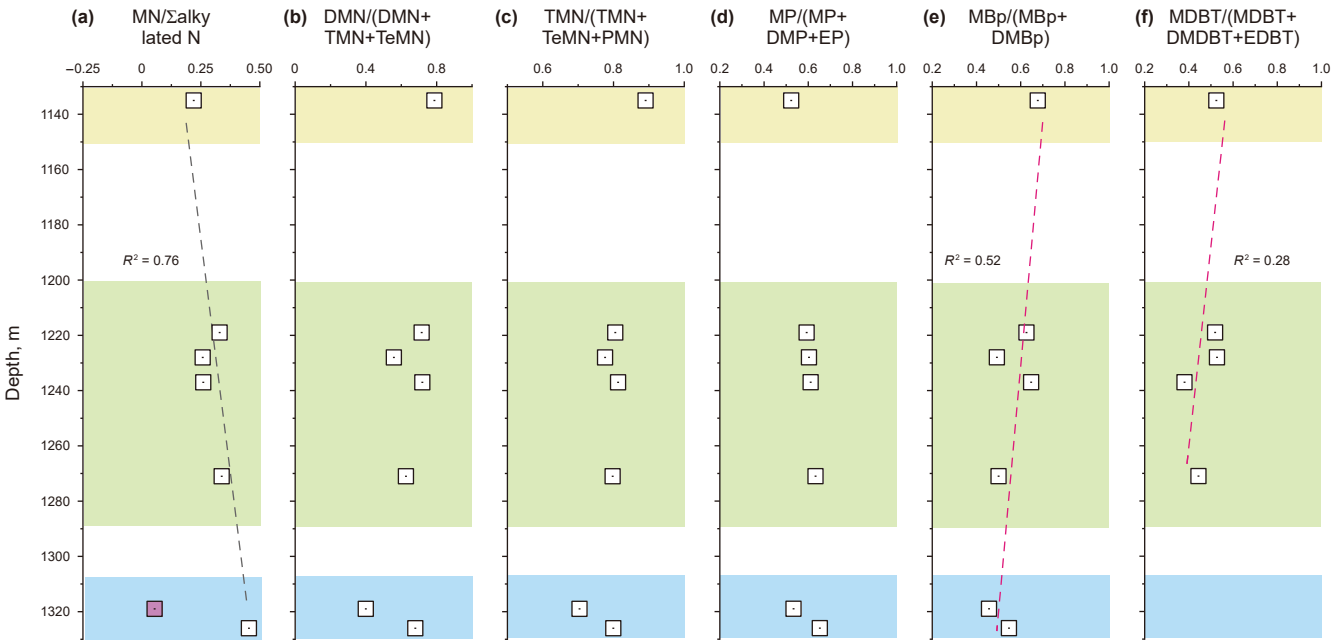

Fig. 11. Trends of demethylation and methylation with depth in the Zhaotong borehole. See Fig. 8 for aromatic compound abbreviations. **(a)** MN/Σalkylnaphthalenes, **(b)** DMN/(DMN + TMN + TeMN), **(c)** TMN/(TMN + TeMN + PMN), **(d)** MP/(MP + DMP + EP), **(e)** MBp/(MBp + DMBp), **(f)** MDBT/(MDBT + DMBT + EDBT).

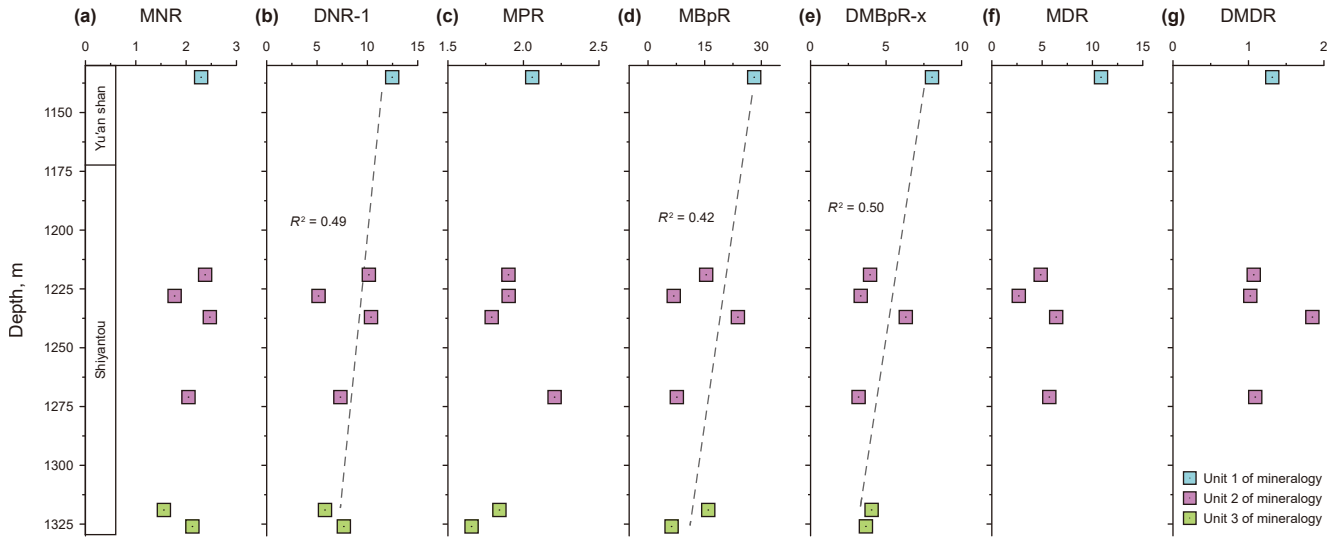

Fig. 12. Variations of thermal-dependent aromatic ratios with depth in the Zhaotong borehole. **(a)** MNR; **(b)** DNR-1; **(c)** MPR; **(d)** MBpR; **(e)** DMBpR-X; **(f)** MDR; **(g)** DMDR. See Table 3 for definition of the ratios.

into this formation (Fig. 1(b)) (Hu et al., 2022; Ning et al., 2021; Wan, 2012). Another more likely possibility is that these anomalous amounts of 1,2,5,6-TeMN and 1,2,5-TMN might be due to benzo-ring fragmentation and aromatisation from triterpenoids or tricyclic terpanes (Püttmann and Villar, 1987; Xu et al., 2004), which were likely derived from microbial OM (Zhang et al., 2007, 2024).

The conjunction of two benzene rings in the biphenyl structure are not delocalised bonds, which are involved in the conjugated system of alkylnaphthalenes and alkylphenanthrenes, and which have the ability to keep these compounds at a lower resonance energy compared to nonconjugated ones (Anslyn and Dougherty, 2004). The alkylated functional group connected with the biphenyl skeleton thus exhibits higher resistance to thermal alteration than those based on the naphthalene or phenanthrene skeletons (Anslyn and Dougherty, 2004). The bond dissociation energy of methyl bonds in alkylated biphenyls are generally greater than that in alkylated naphthalenes or phenanthrenes (Zavitsas, 2003; Anslyn and Dougherty, 2004), resulting in higher temperatures needed for C-C bond cleavage and transmethylation processes. It is suggested that this contributes to the observation that thermally-dependent alkylbiphenyl ratios lag behind the thermally-dependent ratios based on alkylnaphthalenes and alkylphenanthrenes (Figs. 10(e) and 12(d),(e)).

The resonance energy of the benzene rings in compounds increases as further heteroatoms are added (Anslyn and Dougherty, 2004), and the thermal stability of heteroatom-bearing aromatic compounds such as DBTs are weaker (Gantenbein et al., 2017).

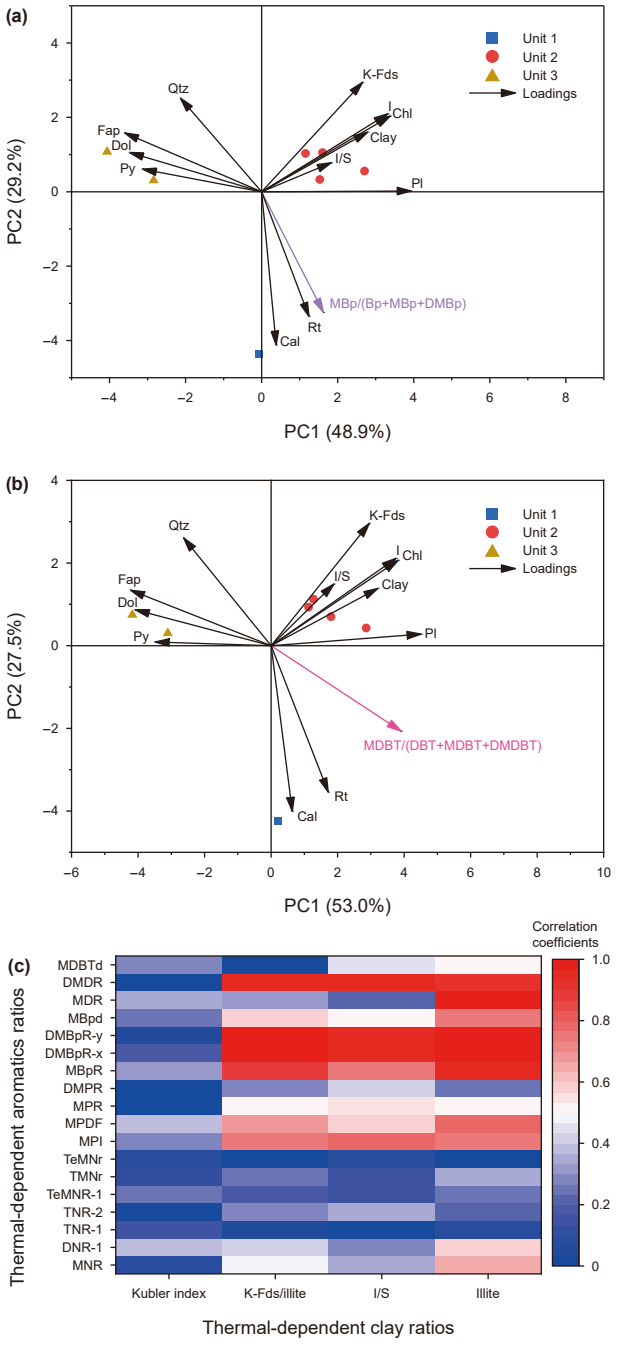

Fig. 13. Principal component analysis of **(a)** MBp/(Bp + MBp + DMBp) and **(b)** MDBT/(DBT + MDBT + DMDBT) with quartz (Qtz), K-feldspar (K-Fds), plagioclase feldspar (Pl), calcite (Cal), dolomite (Dol), pyrite (Py), fluorapatite (Fap), rutile (Rt), clay, illite (I), chlorite (Chl), and mixed-layer illite-smectite (I/S) in three mineralogical units in the samples. PC1 and PC2 are the primary and secondary components in the data, respectively, and the values in the brackets after PC1 and PC2 are the percentage of variance. The length and orientation of the loading coordinates show the contribution of PC1 and PC2, and the angle between each loading represents the correlation between those two factors. **(c)** A heatmap of the correlation coefficients between mineral ratios and a variety of thermally-dependent aromatic ratios. MBpd = MBp/(Bp + MBp + DMBp), MDBTd = MDBT/(DBT + MDBT + DMDBT), for definition of other ratios see Table 3.

However, it is known that sulfur-bearing organic compounds do not behave in a comparable way during increasing thermal maturity as non-heteroatom substituted aromatic compounds, and that different depositional environments and variation in the type of OM are important controls (Fakhraee and Katsev, 2019). The cross plot of MDR versus DMDR consequently fails to provide useful thermal maturity information for this sample set when compared to data from Walton-2 (Fig. 10(f)). Nevertheless, there is a trend of decreasing MDBT/(MDBT + DMBT + EDBT) with depth in the Zhaotong borehole samples (Fig. 11(f)), which is similar to the trend of MBp/(MBp + DMBp) with depth (Fig. 11(e)), indicating that thermal alteration of biphenyls and dibenzothiophenes may have resulted in overall alkylation. The alkylphenanthrene parameter (MP/(MP + DMP + EP) shows overall dealkylation with increasing depth (Fig. 11(d)), whereas similar ratios for the alkylnaphthalenes show no clear trends (Fig. 11(a)–11(c)).

The thermally-dependent alkylbiphenyl and alkyldibenzothiophene ratios generally decrease with depth in the Zhaotong borehole samples (Fig. 12(d), (e)–(g)), as does the DNR-1 ratio (Fig. 12(b)), but with significant scatter. Other ratios have no depth dependence (Fig. 12(a), (c)). This suggests that thermally-dependent alkylbiphenyl and alkyldibenzothiophene ratios may be influenced by factors other than burial heat.

4.2. Relationship between thermal alteration of aromatic compounds and clays

A sufficient input of thermal energy probably did not lead to the disparity in the progress of demethylation or isomeric methyl shifts for the alkylbiphenyls and alkyldibenzothiophenes. Open systems may have a continuous supplement of thermal energy and cation-bearing fluids. However, diagenetic reactions that occur in clays, such as illitisation, are driven by both thermal processes and the influx of monovalent cations such as K^+ and H^+ (Joeleht et al., 2020; Kleber et al., 2015; McIntosh et al., 2021). This could create competing interactions with the thermal cracking of components of the EOM in a closed system, such as corroded pores (Fig. 9(c), (f), (k)). Principal component analysis was performed on three mineralogical units, incorporating mineral proportions in bulk samples, clay mineral proportions in clay fractions, and demethylation intensity ratios of alkylated Bp and alkylated DBT, totalling 13 observed factors (Fig. 13(a) and (b)). The ratios MBp/(Bp + MBp + DMBp) and MDBT/(DBT + MDBT + DMDBT) have unique factors in contrast to the minerals quartz, fluorapatite, dolomite, and pyrite, which have a negative contribution from PC1 and a positive contribution from PC2 (Fig. 13(a) and (b)). This indicates that demethylation or transmethylation of alkylated Bp and alkylated DBT was minimally influenced by these minerals. The clay fractions, plagioclase feldspar, K-feldspar, calcite, and rutile have comparable principal component contributions with MBp/(Bp + MBp + DMBp) and MDBT/(DBT + MDBT + DMDBT), with a positive contribution from PC1 (Fig. 13(a) and (b)). This indicates that the thermal cracking of alkylated Bp and alkylated DBT may have been influenced by the presence of clays, plagioclase feldspar, K-feldspar, calcite, and rutile. The distribution of these minerals is controlled by the transportation and precipitation of K^+, Mg^{2+}, Ca^{2+} ions, which are partly involved in illitisation during diagenesis.

Illite is generally formed by various reactions and intermediates from smectite, and often represents the end-product of clay reactions during diagenesis in sediments (McIntosh et al., 2021). The abundance of illite as a proportion of total clays, and the extent of reaction from smectite to I/S and then to illite is variable, and depends upon the degree of metamorphism that was experienced by the clays (Lázaro, 2007). The cracking intensity of hydrocarbons is diminished in a simulated closed system that included illite-smectite, compared to systems devoid of illite-smectite (Xiao et al., 2010). Therefore, the presence of illite and

smectite may have influenced the cleavage of C-C bonds in the aromatic hydrocarbons.

The coefficient of illite has a strong negative correlation with the thermally-dependent alkylated biphenyl ratios (Fig. 13(c)). The conversion of smectite to illite is triggered by heat, and reaches completion at 100% illite given sufficient thermal energy and free K^+ and H^+ ions (Dong et al., 1997; Joeleht et al., 2020; Lázaro, 2007; Warr and Cox, 2016). Coincidentally, methyl radicals are produced during demethylation and transmethylation, and their chemical state is highly reactive prior to interaction with electron acceptors, such as H^+. This suggests that there may be a competitive relationship between the metamorphic/diagenetic reactions of clays and the thermal alteration of OM, if there were an insufficient supply of thermal energy or cation-bearing fluids.

The relative proportion of I/S might also be linked to the extent of diagenesis or metamorphism. For example, the significant amounts of I/S remaining in some of the sediments of this study (Table 4) suggests a somewhat lower intensity of metamorphic activity and incomplete clay reactions. The thermally-dependent alkylbiphenyl ratios have highly positive coefficients with the amount of I/S (Fig. 13(c)), suggesting that the thermal modification of alkylbiphenyls was highly hindered when a larger amount of smectite was effectively transformed into illite. This suggestion is also supported by the evidence of methylation with depth observed within the burial sequence for the alkylbiphenyls (Fig. 11(e)).

The remaining quantity of K-feldspar in ancient marine sediments can originate both from the original rock after undergoing alteration during early diagenesis, and from detrital influxes (Yuan et al., 2019a). The relative proportions of K-feldspar and illite can be controlled by the severity of weathering, early diagenesis, and clay metamorphism (Ji and Browne, 2000; Joeleht et al., 2020; Yuan et al., 2019a). A low K-feldspar/illite ratio indicates that a sample experienced significant amounts of either weathering or diagenetic alteration, and/or strong metamorphic alteration (Dong et al., 1997; Lázaro, 2007; Yuan et al., 2019a). The association between the K-feldspar/illite ratio and the thermally-dependent alkylated biphenyl ratios results in extremely positive coefficients, 0.875 for MBpR, 0.995 for DMBpR-x, and 0.996 for DMBpR-y (Fig. 13(c)). This suggests that the samples either had a lower intensity of weathering or early diagenetic alteration, and/or a lower degree of metamorphic alteration, and a higher level of thermal alteration of the alkylbiphenyl isomers.

There is no clear correlation between mineral burial alteration and thermal-dependent alkylnaphthalene and alkylphenanthrene ratios (Fig. 13(c)). Both the alkylnaphthalenes and alkylphenanthrenes have a demethylation trend within the burial sequence, based on the MN/$\sum$alkylated naphthalenes and MP/(MP + DMP + EP) ratios (Fig. 11(a),(d)). This indicates that these two groups of alkylated compounds may have been involved in the process of gas generation, and were only slightly affected by illitisation. The MNR and MPR do not vary consistently with depths (Fig. 12(a),(c)), whereas the DNR-1 decreases with increasing depth (Fig. 12(b)). A higher number of alkyl groups in naphthalene reduces the resonance energy of the isomers (Anslyn and Dougherty, 2004), thus helping keep the compounds in highly thermally resistant states. This is shown by the minor reduction of the TMN/(TMN + TeMN + PMN) ratio with depth (Fig. 11(c)), in contrast to the DMN/(DMN + TMN + TeMN) ratio which is essentially invariant (Fig. 11(b)).

The larger proportion of dolomite in the X6 and X7 samples may have resulted in the absence of DBTs in these samples, due to thermal sulfur equilibrium (Nichlaides, 1991) and dolomitisation. The variation of MDR in the depth sequence is different for mineralogical units 1 and 2 (Fig. 12(f)), suggesting that thermal cracking of methyldibenzothiophenes may also have been impeded by illitisation (Fig. 13(c)).

4.3. Possibilities of interaction between aromatic thermal alteration and clay content

The evolution of the molecular structures of aromatic compounds in sediments were proposed to be induced by the decrease of entropy (Page and Jencks, 1971; Anslyn and Dougherty, 2004), which appears to create ordered and compactable compounds by a set of modified molecular structure reactions, including demethylation and aromatisation (Alexander et al., 1985; Asahina and Suzuki, 2018; Budzinski et al., 1993; Craddock et al., 2015; Liu et al., 2024; Mi et al., 2018; Radke et al., 1982b; Vandenbroucke and Largeau, 2007), although the geological processes are complex. When the thermal maturity of OM is defined and attempted to be measured, the type of thermal alteration and the effects of the interaction of OM and minerals should be considered (Yuan et al., 2019b; Cai et al., 2018, 2023). The thermal effect which has been invoked could be attributed to the bond breakage of hydrocarbons (George and Harris, 1977), chemical components exchanging between minerals (Lázaro, 2007), and the absorption or desorption of gas. In this study, the thermal maturity effect that we want to illustrate is associated with the generation of oil or gas, so compounds which have the ability to donate methyl groups during thermal evolution could best help illustrate the thermal maturity level most clearly. The proportion of naphthalene and the alkylnaphthalenes, and phenanthrene and alkylphenanthrenes (Fig. 11(a)–(d)), and also the generally high relative abundance of these compounds relative to other aromatic compounds in many source rocks (Asahina and Suzuki, 2018; Kvalheim et al., 1987) including the samples in this study (Fig. 6(a)), means that these compounds play a major role in demethylation and gas generation. In contrast, the alkylbiphenyls and alkyldibenzothiophenes are present in lower proportions (Fig. 6(a)), have a methylation trend with depth (Fig. 11(e) and (f)), and suggest an anomalously low thermal maturity in the studied samples (Fig. 12(d) and (e)).

Both OM thermal modification and illitisation necessitate the presence of thermal energy (Lázaro, 2007; Pevear, 1999; Warr and Cox, 2016). The process of thermal heating led to illitisation occurring in the gas window in the Zhaotong borehole, as confirmed by the KI and I/S mixed layer values (McIntosh et al., 2021) (Table 4). In the sample from mineralogical unit 1 (X1), there is only a small amount of clay, and a low KI value (Table 4). This indicates that a lesser amount of thermal energy was likely used in the alteration of the clays, and the intensity of illite crystallinity is high (Table 4). The thermal-dependent alkylnaphthalene, alkylphenanthrene, alkylbiphenyl, and alkyldibenzothiophene ratios are significantly higher in sample X1 than for the other samples (Fig. 12), suggesting that these alkylated compounds have undergone extensive thermal modification. The lithology of this sample mostly consists of siltstone, which possesses a porosity advantage over mudstone in terms of the transfer and exchange of ions (Li et al., 2016). This allows for a reasonably open system for clay and OM alteration after burial.

In contrast, mineralogical units 2 and 3 contain a greater quantity of clays and a higher KI (Table 4). This indicates that the amount of thermal energy used for clay modification may have been greater, leading to reduced thermal energy for illite crystallisation. The lithology of mineralogical units 2 and 3 consists predominantly of mudstone (Fig. 1(c)), which typically has a lower porosity than siltstone (Feng et al., 2023). Mudstones commonly maintain microporosity (Fig. 9), but this results from mineral corrosion or OM modification. This type of pore space may have been involved in both the thermal changes of the OM and the alteration of the clays, creating a confined system that allowed for

the interaction between OM and clays due to their close proximity. Illitisation is characterised by the modification of expanded properties, which occur due to the release of exchangeable interlayer cations (e.g., Mg^{2+}, Ca^{2+}) and the retention of K^{+} within the tetrahedral-octahedral-tetrahedral layer (Velde and Meunier, 2008; Mills et al., 2023). Heterovalent substitutions thus lead to a deficiency of positive charge (Velde and Meunier, 2008). H^{+} protons preferentially interact with alumino groups to form Lewis acid sites, and with interlayer water to form Brønsted acid sites (Velde and Meunier, 2008; Du et al., 2021), both of which possess vacant orbitals for the electron-donating pairs of organic molecules. Experimental studies have shown that dibenzothiophene and other S-heterocyclic compounds are effectively adsorbed onto Lewis acid or Brønsted acid sites of clays (Xiao et al., 2008), whereas alkylated biphenyls are preferably retained through hydrophobic sorption in comparison to other moderately hydrophobic PAHs (Moyo et al., 2014).

Therefore, a close spatial association between illite and the EOM provides an opportunity for interactive modifications to occur (Fig. 9(c), (f)). These modifications include the competition of H^{+} ions from the negatively charged surface of the I/S mixed layer, and from the released CH_3^{-} ions during demethylation. In a closed system, both thermal energy and electron acceptors are necessary for the processes of illitisation and demethylation. This suggests that there may have been a competitive relationship between illitisation and thermal alteration of the aromatic compounds. This relationship is further supported by the coefficient correlations shown in Fig. 13(c). Nevertheless, to further test this hypothesis, it will be necessary to sample a variety of rocks and sediments from different geological periods, and conduct laboratory simulations in order to ensure additional validation.

5. Conclusions

A comprehensive examination of XRD, GC-MS, and SEM data from early Cambrian samples from a borehole in the Yangtze Platform was carried out to investigate the thermal maturity of the EOM and the mineral composition, as well as the interaction of these during burial.

(1) The aromatic compounds that were identified mainly have a β isomerisation preference, indicating that the aromatic compounds underwent significant thermal alteration. Multiple cross plots of the C_1 and C_2 alkylnaphthalenes and alkylphenanthrenes indicate a gas window thermal maturity, which is consistent with the kerogen thermal maturity in the Yangtze Platform. However, the thermal-maturity dependent ratios from some C_3 and C_4 alkylnaphthalenes, C_1 and C_2 alkylbiphenyls, and C_1 alkyldibenzothiophenes are diverse and delayed.

(2) The thermal maturity-dependent ratios based on methylnaphthalenes and methylphenanthrenes have comparable values throughout the three mineralogical units at various burial depths. In contrast, the thermal maturity-dependent ratios derived from C_2 alkylnaphthalenes, C_1 alkylbiphenyls, and alkyldibenzothiophenes have highest values in the shallowest unit 1, followed by unit 2, and the lowest values in unit 3, which corresponds to the samples with the most extensive burial history.

(3) The illite in unit 1 has higher crystallinity, while in units 2 and 3 the illite has lower crystallinity, indicating that the clays in units 2 and 3 were subjected to less heating. In addition based on SEM analysis, clays such as illite and chlorite are closely associated with OM in a spatial manner for both units 2 and 3.

(4) In order to investigate the potential impact of illitisation on the thermal alteration of the alkylated aromatics, a series of correlation analyses were conducted. These analyses focused on examining the relationship between illite-associated ratios (such as the proportion of illite and mixed-layer illite-smectite (I/S), and the K-feldspar/illite ratio), and thermal-dependent aromatic ratios. The thermal ratios derived from alkylbiphenyls and alkyldibenzothiophenes have significant negative correlations with the proportion of illite in clay, while there are substantial positive correlations with the proportions of I/S and the K-feldspar/illite ratio.

(5) Consequently, we hypothesise that the process of illitisation may have an impact on the demethylation of some alkylated PAHs, such as alkylbiphenyls and alkyldibenzothiophenes. Firstly, a potential possibility is that both demethylation and illitisation require heat evolution. Secondly, an enhanced H^{+} proton-bearing surface (i.e., Lewis acid and Brønsted acid sites) due to illitisation may favour absorption of alkylated dibenzothiophenes. Alkylated biphenyls are preferentially sustained in the interlayer of I/S by hydrophobic sorption relative to other moderately hydrophobic PAHs. Alkylated biphenyls and alkylated dibenzothiophenes are thus highly captured and targeted during illitisation. A third aspect pertains to lithology. Units 2 and 3 have a greater quantity of clays compared to unit 1, resulting in a denser mudstone matrix, in contrast to the silty sand in unit 1. Units 2 and 3 are thus a relatively closed system, which possesses insufficient thermal energy and ion-bearing fluids, resulting in competition between illitisation of clays and demethylation of alkylated biphenyls and alkylated dibenzothiophenes.

(6) Overall, thermal ratios derived from alkylnaphthalenes and alkylphenanthrenes can be considered dependable for interpreting thermal maturity, especially for mudstones. The illitisation process in clay-bearing sediments is associated with the thermal modification of alkylbiphenyls and alkyldibenzothiophenes. We propose that ratios of methylnaphthalenes and methylphenanthrenes are highly valuable thermal maturity indicators for early Cambrian mudstones on the Yangtze Platform. Care must be taken with the application of thermally-dependent alkylated biphenyl ratios for rocks with fractures, and also for thermally-dependent alkylated dibenzothiophene ratios for rocks originating from significantly diverse depositional environments.

CRediT authorship contribution statement

Qian-Nan Xu: Writing – review & editing, Writing – original draft, Visualization, Validation, Software, Methodology, Investigation, Formal analysis, Data curation, Conceptualization. **Yan-Ming Zhu:** Writing – review & editing, Supervision, Resources, Funding acquisition. **Shang-Bin Chen:** Writing – review & editing. **Yu Liu:** Writing – review & editing. **Xiao-Qi Wang:** Writing – review & editing. **Fu-Hua Shang:** Writing – review & editing. **Simon C. George:** Writing – review & editing, Validation, Supervision, Resources, Methodology, Funding acquisition, Conceptualization.

Declaration of competing interest

The authors declare that they have no known competing financial interests or personal relationships that could have appeared to influence the work reported in this paper.

Acknowledgements

We thank Yunnan Coalbed Methane Resources Exploration and Development Co., Ltd for providing the borehole samples. We thank Chong-Yu Wu for advising about the clay fractionation and XRD data identification. We thank Dr. Sean Murray for the Aeris XRD machine and HighScore software induction. Qian-Nan Xu thanks Macquarie University for providing support as a visiting PhD student. This work is supported by the China Scholarship Council (Grant No. 202206420028), and the National Natural Science Foundation of China (Grant No. 42072199), the National Natural Science Foundation of China (No. 42102225), the China Postdoctoral Science Foundation (2025M770883), and funding from the Organic Geochemistry Lab of Emeritus Professor Simon C. George.

References

Abubakar, Y., Taylor, K.G., Coker, V., Wogelius, R.A., van Dongen, B.E., 2022. Fundamental controls on organic matter preservation in organic- and sulfur-rich hydrocarbon source rocks. Mar. Petrol. Geol. 141, 105684. https://doi.org/10.1016/j.marpetgeo.2022.105684.

Agrawal, V., Sharma, S., 2018. Improved kerogen models for determining thermal maturity and hydrocarbon potential of shale. Sci. Rep. 8, 17465. https://doi.org/10.1038/s41598-018-35560-8.

Ahmat, A.M., Boussafir, M., Le Milbeau, C., Guegan, R., Valdès, J., Guiñez, M., Sifeddine, A., Le Forestier, L., 2016. Organic matter-clay interaction along a seawater column of the Eastern Pacific upwelling system (Antofagasta Bay, Chile): Implications for source rock organic matter preservation. Mar. Chem. 179, 23–33. https://doi.org/10.1016/j.marchem.2016.01.003.

Ahmed, M., George, S.C., 2004. Changes in the molecular composition of crude oils during their preparation for GC and GC-MS analyses. Org. Geochem. 35, 137–155. https://doi.org/10.1016/j.orggeochem.2003.10.002.

Alexander, R., Cumbers, K.M., Kagi, R.I., 1986. Alkylbiphenyls in ancient sediments and petroleums. Org. Geochem. 10, 841–845. https://doi.org/10.1016/s0146-6380(86)80021-3.

Alexander, R., Kagi, R.I., Rowland, S.J., Sheppard, P.N., Chirila, T.V., 1985. The effects of thermal maturity on distributions of dimethylnaphthalenes and trimethylnaphthalenes in some ancient sediments and petroleums. Geochem. Cosmochim. Acta 49, 385–395. https://doi.org/10.1016/0016-7037(85)90031-6.

Alexander, R., Kagi, R.I., Singh, R.K., Sosrowidjojo, I.B., 1994. The effect of maturity on the relative abundances of cadalene and isocadalene in sediments from the Gippsland Basin, Australia. Org. Geochem. 21, 115–120. https://doi.org/10.1016/0146-6380(94)90148-1.

Anslyn, E.V., Dougherty, D.A., 2004. Modern Physical Organic Chemistry, First ed. Sausalito, California.

Asahina, K., Suzuki, N., 2018. Methylated naphthalenes as indicators for evaluating the source and source rock lithology of degraded oils. Org. Geochem. 124, 46–62. https://doi.org/10.1016/j.orggeochem.2018.06.012.

Awan, R.S., Liu, C.L., Dehao, F., Zang, Q.B., Wu, Y.P., Ali, S., 2023. Origin of organic matter and depositional characteristics of early Cambrian Niutitang Formation from South China: New insights using molecular fossils. Geo. J. 58, 298–314. https://doi.org/10.1002/gj.4593.

Awan, R.S., Liu, C.L., Gong, H.W., Dun, C., Tong, C., Chamssidini, L.G., 2020. Paleo-sedimentary environment in relation to enrichment of organic matter of early Cambrian black rocks of Niutitang Formation from Xiangxi area China. Mar. Petrol. Geol. 112. https://doi.org/10.1016/j.marpetgeo.2019.104057.

Baruah, B., Tiwari, P., 2022. Compositional and kinetic study of thermal degradation of kerogen using TG-FTIR, NMR, and microscopic study. AlChE J. 68, e17396. https://doi.org/10.1002/aic.17396.

Brindley, G.W., Brown, G., 1980. Crystal Structure of Clay Minerals and their x-ray Identification. Mineralogical Society of Great Britain and Ireland, Britain.

Budzinski, H., Garrigues, P., Radke, M., Connan, J., Oudin, J.L., 1993. Thermodynamic calculations on alkylated phenanthrenes-geochemical applications to maturity and origin of hydrocarbons. Org. Geochem. 20, 917–926. https://doi.org/10.1016/0146-6380(93)90103-i.

Cai, C., Garrigues, P., Radke, M., Connan, J., Oudin, J.L., 2023. Thermodynamic calculations on alkylated phenanthrenes - geochemical applications to maturity and origin of hydrocarbons. Org. Geochem. 20, 917–926. https://doi.org/10.1016/0146-6380(93)90103-i.

Bureau of geology and mineral resources of Yunnan province, 1990. Regional geology of Yunnan province, First ed. Beijing, China.

Cai, C., Cai, J., Du, J., Lei, J., Lei, T., Wang, X., Li, Z., 2023. Multistage hydrocarbon generation of saline lacustrine source rocks in hydrous pyrolysis: insights from clay mineral–organic matter interactions. ACS Omega 8, 14710–14729.

Chen, X., Ling, H.F., Vance, D., Shields-Zhou, G.A., Zhu, M.Y., Poulton, S.W., Och, L.M., Jiang, S.Y., Li, D., Cremonese, L., Archer, C., 2015. Rise to modern levels of ocean oxygenation coincided with the Cambrian radiation of animals. Nat. Commun. 6, 1–7. https://doi.org/10.1038/ncomms8142.

Coates, J.D., Anderson, R.T., Lovley, D.R., 1996. Oxidation of polycyclic aromatic hydrocarbons under sulfate-reducing conditions. Appl. Environ. Microbiol. 62, 1099–1101. https://doi.org/10.1128/aem.62.3.1099-1101.1996.

Craddock, P.R., Doan, T.V.L., Bake, K., Polyakov, M., Charsky, A.M., Pomerantz, A.E., 2015. Evolution of kerogen and bitumen during thermal maturation via semi-open pyrolysis investigated by infrared spectroscopy. Energy Fuel. 29, 2197–2210. https://doi.org/10.1021/ef5027532.

Cuadros, J., 2006. Modeling of smectite illitization in burial diagenesis environments. Geochem. Cosmochim. Acta 70 (16), 4181–4195. https://doi.org/10.1016/j.gca.2006.06.1372.

Cumbers, K.M., Alexander, R., Kagi, R.I., 1987. Methylbiphenyl, ethylbiphenyl and dimethylbiphenyl isomer distributions in some sediments and crude oils. Geochem. Cosmochim. Acta 51, 3105–3111. https://doi.org/10.1016/0016-7037(87)90121-9.

Dong, H., Peacor, D.R., Freed, R.L., 1997. Phase relations among smectite, R1 illite-smectite, and illite. Am. Mineral. 82, 379–391. https://doi.org/10.2138/am-1997-3-416.

Du, J.Z., Cai, J.G., Chao, Q., Song, M.S., Wang, X.J., 2021. Variations and geological significance of solid acidity during smectite illitization. Appl. Clay Sci. 204, 106035. https://doi.org/10.1016/j.clay.2021.106035.

Eberl, D.D., Velde, B., 1989. Beyond the Kubler index. Clay Miner. 24, 571–577. https://doi.org/10.1180/claymin.1989.024.4.01.

Fakhraee, M., Katsev, S., 2019. Organic sulfur was integral to the Archean sulfur cycle. Nat. Commun. 10, 4556. https://doi.org/10.1038/s41467-019-12396-y.

Fang, R.H., Li, M.J., Wang, T.G., Zhang, L.W., Shi, S.B., 2015. Identification and distribution of pyrene, methylpyrenes and their isomers in rock extracts and crude oils. Org. Geochem. 83–84, 65–76. https://doi.org/10.1016/j.orggeochem.2015.03.003.

Fang, X.Y., Wu, L.L., Geng, A.S., Deng, Q., 2019. Formation and evolution of the Ediacaran to Lower Cambrian black shales in the Yangtze Platform, South China. Palaeogeogr. Palaeoclimatol. Palaeoecol. 527, 87–102. https://doi.org/10.1016/j.palaeo.2019.04.025.

Feng, G., Li, W., Zhu, Y., Wang, Y., Song, Y., Zheng, S., Shang, F., 2023. Scale-dependent fractal properties and geological factors for the pore structure in shale: insights from field emission scanning electron microscopy and fluid intrusion. Energy Fuel. 37, 16519–16535. https://doi.org/10.1021/acs.energyfuels.3c02833.

Gantenbein, M., Wang, L., Al-jobory, A.A., Ismael, A., Lambert, C., Hong, W., Bryce, M., 2017. Quantum interference and heteroaromaticity of para- and meta-linked bridged biphenyl units in single molecular conductance measurements. Sci. Rep. 7, 1794. https://doi.org/10.1038/s41598-017-01903-0.

George, J.H., Harris, H.G., 1977. Mathematical modeling of in situ oil shale retorting. SIAM J. Numer. Anal. 14, 137–151. http://www.jstor.org/stable/2156625.

George, S.C., Ahmed, M., 2002. Use of aromatic compound distributions to evaluate organic maturity of the Proterozoic middle Velkerri formation, McArthur Basin, Australia, the sedimentary Basins of Western Australia. Proceedings of the Petroleum Exploration Society of Australia Symposium. Perth, Australia, pp. 253–270.

George, S.C., Lisk, M., Eadington, P.J., Quezada, R.A., Krieger, F.W., Greenwood, P.F., Wilson, M.A., 1996. Comparison of palaeo oil charges with currently reservoired hydrocarbons using the geochemistry of oil-bearing fluid inclusions. In: Comparison of palaeo oil charges with currently reservoired hydrocarbons using the geochemistry of oil-bearing fluid inclusions. SPE paper 36980, Society of Petroleum Engineers, Asia Pacific Oil and Gas Conference, 28–31, Adelaide, Australia, pp. 159–171. https://doi.org/10.2118/36980-MS.

George, S.C., Ruble, T.E., Dutkiewicz, A., Eadington, P.J., 2001. Assessing the maturity of oil trapped in fluid inclusions using molecular geochemistry data and visually-determined fluorescence colours. Appl. Geochem. 16, 451–473. https://doi.org/10.1016/s0883-2927(00)00051-2.

Gharrabi, M., Velde, B., Sagon, J.P., 1998. The transformation of illite to muscovite in pelitic rocks: constraints from X-ray diffraction. Clays Clay Miner. 46, 79–88. https://doi.org/10.1346/ccmn.1998.0460109.

Guo, H., Liu, M., Wang, Y., Wang, Q., Liu, J., Peng, P., 2022. Characterization of chemical and carbon isotopic compositions of gases during thermochemical sulfate reduction and implications for gas origin and content. Sci. Rep. 12, 9118. https://doi.org/10.1038/s41598-022-12017-3.

Hall, P.A., 2012. Elemental, isotopic and molecular signatures of early Cambrian marine sediments and a phantom petroleum system in South Australia. Geology and Geophysics, School of Earth and Environmental Science. Faculty of Science. University of Adelaide, p. 753.

Han, S.J., Löhr, S.C., Abbott, A.N., Baldermann, A., Voigt, M., Yu, B.S., 2022. Authigenic clay mineral evidence for restricted, evaporitic conditions during the emergence of the Ediacaran Doushantuo Biota. Commun. Earth Environ. 3, 165. https://doi.org/10.1038/s43247-022-00495-6.

He, C., Chen, H., Xiao, X., Liu, X., Su, A., 2023. Differential shale gas generation in the lower Cambrian Qiongzusi stage in the Middle-Upper Yangtze region. Earth Sci. Front. 30, 44–65. https://doi.org/10.13745/j.esf.sf.2022.5.33 (Chinese in English abstract).

He, K., Zhang, S., Wang, X., Mi, J., Mao, R., Hu, G., 2013. Effect of gas generation from insitu cracking of residual bitumen in source on hydrocarbon generation from organic matter. Acta Petrol. Sin. 34, 57–64. https://doi.org/10.7623/syxb2013S1006 (in Chinese).

Hu, D., Sun, L., Xu, Y., Zhang, Xingliang, Zhang, Xiaolin, Shen, Y., 2025. Increased oxygenation during the peak Cambrian explosion: evidence from global carbon

isotope records. Chem. Geol. 690, 122890. https://doi.org/10.1016/j.chemgeo.2025.122890.
Hu, L., Zhu, Y., Chen, S., Chen, J., Wang, Y., 2012. Resource potential analysis of shale gas in Lower Cambrian Qiongzhusi formation in middle and upper Yangtze region. J. China Coal Soc. 37, 1871–1877 (in Chinese).
Hu, Z., Gao, Z., Liu, Z., Jiang, W., Wei, D., Li, Y., 2022. Characteristics of Cambrian tectonic-lithofacies paleogeography in China and the controls on hydrocarbons. J. Petrol. Sci. Eng. 214, 110473. https://doi.org/10.1016/j.petrol.2022.110473.
Hutskalova, V., Sparr, C., 2024. Aromatic ring-opening metathesis. Nature 638, 697–703. https://doi.org/10.1038/s41586-024-08472-z.
Ji, J., Browne, P.R.L., 2000. Relationship between illite crystallinity and temperature in active geothermal systems of New Zealand. Clays Clay Miner. 48, 139–144. https://doi.org/10.1346/CCMN.2000.0480117.
Jiang, L., Zhao, M., Shen, A., Huang, L., Chen, D., Cai, C., 2022. Pulses of atmosphere oxygenation during the Cambrian radiation of animals. Earth Planet Sci. Lett. 590, 117565. https://doi.org/10.1016/j.epsl.2022.117565.
Joeleht, A., Kirsimae, K., Somelar, P., 2020. Illitization of the Lower Cambrian (Terreneuvian) blue clay in the northern Baltic palaeobasin. Est. J. Earth Sci. 69, 200–213. https://doi.org/10.3176/earth.2020.14.
Kennedy, M.J., Pevear, D.R., Hill, R.J., 2002. Mineral surface control of organic carbon in black shale. Science 295, 657–660. https://doi.org/10.1126/science.1066611.
Kleber, M., Eusterhues, K., Keiluweit, M., Mikutta, C., Mikutta, R., Nico, P.S., 2015. Mineral-organic associations: formation, properties, and relevance in soil environments. In: Sparks, D.L. (Ed.), Adv. Agron, pp. 1–140.
Kruge, M.A., 2000. Determination of thermal maturity and organic matter type by principal components analysis of the distributions of polycyclic aromatic compounds. Int. J. Coal Geol. 43, 27–51. https://doi.org/10.1016/s0166-5162(99)00053-1.
Kvalheim, O.M., Christy, A.A., Telnæs, N., Bjørseth, A., 1987. Maturity determination of organic-matter in coals using the methylphenanthrene distribution. Geochem. Cosmochim. Acta 51, 1883–1888. https://dio.org/10.1016/0016-7037(87)90179-7.
Lavik, G., Stűhrmann, T., Brűchert, V., Van der Plas, A., Mohrholz, V., Lam, P., Mußmann, M., Fuchs, B.M., Amann, R., Lass, U., Kuypers, M.M.M., 2008. Detoxification of sulphidic African shelf waters by blooming chemolithotrophs. Nature 457, 581–584. https://doi.org/10.1038/nature07588.
Lázaro, B.B., 2007. Illitization processes : Series of dioctahedral clays and mechanisms of formation. In: Jimenez-Millan, F.N.y.J. (Ed.), Seminarios De La Sociedad Espanola De Mineralogia. Sociedad Espanola de Mineralogia, Spain, pp. 31–38.
Li, A., Ding, W., He, J., Dai, P., Yin, S., Xie, F., 2016. Investigation of pore structure and fractal characteristics of organic-rich shale reservoirs: A case study of Lower Cambrian Qiongzhusi Formation in Malong block of eastern Yunnan Province, South China. Mar. Petrol. Geol. 70, 46–57. https://doi.org/10.1016/j.marpetgeo.2015.11.004.
Li, G., Wei, F., Cong, P., 2025. The earliest calcified cyanobacteria from the Cambrian Terreneuvian at the western margin of the Yangtze Plate, China. Lethaia 58, 1–14. https://dio.org/10.18261/let.58.2.3.
Li, J.R., Yang, Z., Wu, S.T., Pan, S.Q., 2021. Key issues and development direction of petroleum geology research on source rock strata in China. Adv. Geo-Energy Res. 5, 121–126. https://doi.org/10.46690/ager.2021.02.02.
Liang, C., Ji, S., Cao, Y., Liu, K., Wu, J., Hao, F., 2024. Characteristics, origins, and significance of pyrites in deep-water shales. Sci. China Earth Sci. 67 (2), 313–342. https://doi.org/10.1007/s11430-022-1200-0.
Lindsay, A.M., Michael, H.H., Chen, J., Nancy, W.H., 2015. Stratigraphic controls of soft-bodied fossil occurrences in the Cambrian Chengjiang biota Lagerstätte, Maotianshan shale, Yunnan Province, China. Palaeogeogr. Palaeoclimatol. Palaeoecol. 420, 96–115. https://doi.org/10.1016/j.palaeo.2014.11.006.
Liu, Y., Xie, S.Y., Feng, G.J., Su, C., Xu, Q.N., Gao, T.W., 2024. Evolution of kerogen structure during the carbonization stage. Org. Geochem. 190, 104743. https://doi.org/10.1016/j.orggeochem.2024.104743.
Liu, Z., Gao, B., Feng, D., Cui, X., Du, W., Wang, Y., Li, D., 2017. Mineral composition of the Lower Cambrian black shale in the Upper Yangtze region and its significance in oil and gas exploration. Nat. Gas. Ind. B. 4, 340–345. https://doi.org/10.1016/j.ngib.2017.09.003.
Machel, H.G., 2001. Bacterial and thermochemical sulfate reduction in diagenetic settings — old and new insights. Sediment. Geol. 140 (1–2), 143–175. https://doi.org/10.1016/S0037-0738(00)00176-7.
Manda, B., Kachira, R., Mohamed, H., George, S.C., 2023. The organic geochemistry of Permian high latitude sediments in two boreholes in the southern Sydney Basin, New South Wales, Australia. Mar. Petrol. Geol. 154, 106316. https://doi.org/10.1016/j.marpetgeo.2023.106316.
Martínez, M., Lorenzo, E., Morato, A., Gamboa, A., 2020. Distribution and geochemical significance of biphenyls and related bicyclic aromatic structures in oils from Ancon oilfield (Tertiary Progreso Basin), Ecuador. Geochem. J. 54, 139–143. https://doi.org/10.2343/geochemj.2.0598.
McIntosh, J.A., Tabor, N.J., Rosenau, N.A., 2021. Mixed-layer illite-smectite in Pennsylvanian-aged paleosols: assessing sources of illitization in the Illinois Basin. Minerals 11, 2. https://doi.org/10.3390/min11020108.
Meng, K., Zhang, T.W., Shao, D.Y., Liu, X.Y., Song, H., Peng, H., 2024. Assessment of thermal maturity in Lower Cambrian organic-rich shale in South China using integrated optical reflectance and Raman spectroscopy of pyrobitumen. Mar. Petrol. Geol. 160, 106609. https://doi.org/10.1016/j.marpetgeo.2023.106609.
Mi, J.K., Wang, H.T., He, K., Bai, J.F., Liu, C.Y., 2018. Demethylation as a mechanism for isotopic reversals of shale gas generated at over maturity. J. Anal. Appl. Pyrolysis 135, 361–368. https://doi.org/10.1016/j.jaap.2018.08.015.
Mills, M.M., Sanchez, A.C., Boisvert, L., Payne, C.B., Ho, T.A., Wang, Y., 2023. Understanding smectite to illite transformation at elevated (>100 °C) temperature: effects of liquid/solid ratio, interlayer cation, solution chemistry and reaction time. Chem. Geol. 615, 121214. https://doi.org/10.1016/j.chemgeo.2022.121214.
Moore, W.J., 1972. Physical Chemistry, Fifth. Longman Group Limited, London.
Mosser-Ruck, R., Pironon, J., Cathelineau, M., Trouiller, A., 2001. Experimental illitization of smectite in a K-rich solution. Eur. J. Mineral 13 (5), 829–840. https://doi.org/10.1127/0935-1221/2001/0013/0829.
Moyo, F., Tandlich, R., Wilhelmi, B.S., Balaz, S., 2014. Sorption of hydrophobic organic compounds on natural sorbents and organoclays from aqueous and non-aqueous solutions: A mini-review. Int. J. Environ. Res. Publ. Health 11, 5020–5048. https://doi.org/10.3390/ijerph110505020.
National Energy Administration, B., 2010. Analysis Method for Clay Minerals and Ordinary Non-clay Minerals in Sedimentary Rocks by the X-ray Diffraction. Petroleum Industry Press, China, pp. 3–39.
Nichlaides, S., 1991. Dolomitization of the early to middle Cambrian carbonate rocks of Georgina Basin, Northern Territory, Australia. Petroleum Geology and Geophysics. The University of Adelaide, p. 224.
Ning, Y., Tang, H., Smith, J.V., Zhang, B., Shen, P., Zhang, G., 2021. Study of the in situ stress field in a deep valley and its influence on rock slope stability in Southwest China. Bull. Eng. Geol. Environ. 80, 3331–3350. https://doi.org/10.1007/s10064-020-02094-1.
Noorian, Y., Farkas, J., Collins, A.S., Delle Piane, C., Hall, P.A., 2025. Controls on organic-rich shale formation in the Mesoproterozoic Beetaloo Sub-basin, Northern Territory, Australia: insights from biogeochemistry and mineralogy. Precambr. Res. 427, 7869, 7869.
Ogbesejana, A., Bello, O., Uduma, U., 2019. Occurrence of biphenyl and alkylbiphenyls in source rocks from Tertiary Niger delta basin, Nigeria. ChemSearch J 9, 29–37.
Page, M.I., Jencks, W.P., 1971. Entropic contributions to rate accelerations in enzymic and intramolecular reactions and the chelate effect. Proc. Natl. Acad. Sci. USA 68 (8), 1678–1683. https://doi.org/10.1073/pnas.68.8.1678.
Peng, W., Liu, Q., Hu, G., Lv, Y., Meng, Q., Guo, F., Guan, H., 2020. A new interpretation of carbon isotope series reverse of highly-over mature alkane gases: Demethylation of aromatic hydrocarbons. Earth Sci. 45, 1308–1314. https://doi.org/10.3799/dqkx.2019.133.
Pevear, D.R., 1999. Illite and hydrocarbon exploration. Proc. Natl. Acad. Sci. USA 96, 3440–3446. https://doi.org/10.1073/pnas.96.7.3440.
Poppe, L.J., Paskevich, V., Hathaway, J., Blackwood, D., 2001. A laboratory manual for X-ray powder diffraction. US Geological Survey Open File Report 1, 1–88.
Püttmann, W., Villar, H., 1987. Occurrence and geochemical significance of 1,2,5,6-tetramethylnaphthalene. Geochem. Cosmochim. Acta 51, 3023–3029. https://doi.org/10.1016/0016-7037(87)90375-9.
Qiao, Y., Cui, L., Xing, G., Fu, D., Chang, C., Gaines, R., Zhang, X., 2024. Thermal history of Cambrian Burgess shale-type deposits: New insights from the early Cambrian Chengjiang and Qingjiang fossils of South China. J. Earth Sci. 35 (4), 1215–1223. https://doi.org/10.1007/s12583-023-1921-2.
Qiu, N.S., Liu, W., Fu, X.D., Li, W.Z., Xu, Q.C., Zhu, C.Q., 2021. Maturity evolution of Lower Cambrian Qiongzhusi Formation shale of the Sichuan Basin. Mar. Petrol. Geol. 128, 105061. https://doi.org/10.1016/j.marpetgeo.2021.105061.
Radke, M., Welte, D.H., Willsch, H., 1982a. Geochemical study on a well in the Western Canada basin - relation of the aromatic distribution pattern to maturity of organic-matter. Geochem. Cosmochim. Acta 46, 1–10. https://doi.org/10.1016/0016-7037(82)90285-X.
Radke, M., Welte, D.H., Willsch, H., 1986. Maturity parameters based on aromatic hydrocarbons: influence of the organic-matter type. Org. Geochem. 10, 51–63. https://doi.org/10.1016/0146-6380(86)90008-2.
Radke, M., Willsch, H., Leythaeuser, D., Teichmuller, M., 1982b. Aromatic components of coal: relation of distribution pattern to rank. Geochem. Cosmochim. Acta 46, 1831–1848. https://doi.org/10.1016/0016-7037(82)90122-3.
Rahman, H.M., Kennedy, M., Löhr, S., Dewhurst, D.N., 2017. Clay-organic association as a control on hydrocarbon generation in shale. Org. Geochem. 105, 42–55. https://doi.org/10.1016/j.orggeochem.2017.01.011.
Robison, C.R., van Gijzel, P., Darnell, L.M., 2000. The transmittance color index of amorphous organic matter: A thermal maturity indicator for petroleum source rocks. Int. J. Coal Geol. 43, 83–103. https://doi.org/10.1016/S0166-5162(99)00055-5.
Saleh, F., Qi, C., Buatois, L.A., Mángano, M.G., Paz, M., Vaucher, R., Zheng, Q., Hou, X.G., Gabbott, S.E., Ma, X., 2022. The Chengjiang biota inhabited a deltaic environment. Nat. Commun. 13, 1–9. https://doi.org/10.1038/s41467-022-29246-z.
Shu, D., 2008. Cambrian explosion: birth of tree of animals. Gondwana Res. 14, 219–240. https://doi.org/10.1016/j.gr.2007.08.004.
Steiner, M., Zhu, M.Y., Weber, B., Geyer, G., 2001. The Lower Cambrian of eastern Yunnan: Trilobite-based biostratigraphy and related faunas. Acta Palaeontol. Sin. 40, 63–79.
Sun, H., Zhao, F., Steiner, M., Li, G., Na, L., Pan, B., Yin, Z., Zeng, H., Van Iten, H., Zhu, M., 2020. Skeletal faunas of the Lower Cambrian Yu'anshan formation, eastern Yunnan, China: Metazoan diversity and community structure during

the Cambrian Age 3. Palaeogeogr. Palaeoclimatol. Palaeoecol. 542, 109580. https://doi.org/10.1016/j.palaeo.2019.109580.
Svensson, P.D., Hansen, S., 2010. Intercalation of smectite with liquid ethylene glycol - resolved in time and space by synchrotron X-ray diffraction. Appl. Clay Sci. 48, 358–367. https://doi.org/10.1016/j.clay.2010.01.006.
Tang, B.N., Zhu, C.Q., Xu, M., Chen, T.G., Hu, S.B., 2019. Thermal conductivity of sedimentary rocks in the Sichuan Basin, Southwest China. Energy Explor. Exploit. 37, 691–720. https://doi.org/10.1177/0144598718804902.
Tannenbaum, E., Kaplan, I.R., 1985. Role of minerals in the thermal alteration of organic-matter .1. Generation of gases and condensates under dry condition. Geochem. Cosmochim. Acta 49, 2589–2604. https://doi.org/10.1016/0016-7037(85)90128-0.
Tao, S., Wang, Y.B., Tang, D.Z., Xu, H., 2012. Hydrocarbon-generation in Cambrian-Silurian high- to over- mature source rocks, Middle and Upper Yangtze region, China. Energy Explor. Exploit. 30, 19–41. https://doi.org/10.1260/0144-5987.30.1.19.
Tiem, V.T.A., Horsfield, B., Sykes, R., 2008. Influence of in-situ bitumen on the generation of gas and oil in New Zealand coals. Org. Geochem. 39, 1606–1619. https://doi.org/10.1016/j.orggeochem.2008.07.005.
Tosca, N.J., Johnston, D.T., Mushegian, A., Rothman, D.H., Summons, R.E., Knoll, A.H., 2010. Clay mineralogy, organic carbon burial, and redox evolution in Proterozoic oceans. Geochem. Cosmochim. Acta 74, 1579–1592. https://dio.org/10.1016/j.gca.2009.12.001.
Uruowhe, B.O., 2021. The Timing of smectite-to-illite Transformation in Cretaceous Rocks of Powder River Basin, Department of Geosciences. Georgia State University, pp. 41–50.
van Aarssen, B.G.K., Bastow, T.P., Alexander, R., Kagi, R.I., 1999. Distributions of methylated naphthalenes in crude oils: Indicators of maturity, biodegradation and mixing. Org. Geochem. 30, 1213–1227. https://doi.org/10.1016/s0146-6380(99)00097-2.
van Duin, A.C.T., Baas, J.M.A., van de Graaf, B., de Leeuw, J.W., Bastow, T.P., Alexander, R., 1997. Comparison of calculated equilibrium mixtures of alkylnaphthalenes and alkylphenanthrenes with experimental and sedimentary data; the importance of entropy calculations. Org. Geochem. 26, 275–280. https://doi.org/10.1016/s0146-6380(97)00013-2.
Vandenbroucke, M., Largeau, C., 2007. Kerogen origin, evolution and structure. Org. Geochem. 38, 719–833. https://doi.org/10.1016/j.orggeochem.2007.01.001.
Velde, B., Meunier, A., 2008. The Origin of Clay Minerals in Soils and Weathered Rocks, first ed. Springer, Berlin, Heidelberg.
Verdel, C., Niemi, N., van der Pluijm, B., 2011. Variations in the illite to muscovite transition related to metamorphic conditions and detrital muscovite content: insight from the Paleozoic passive margin of the Southwestern United States. J. Geol. 119, 419–437. https://doi.org/10.1086/660086.
Wan, T., 2012. Tectonics of the Mesoproterozoic, Neoproterozoic and early Cambrian (1.8 Ga–513 Ma). In: Wan, T. (Ed.), The Tectonics of China: Data, Maps and Evolution. Springer Berlin Heidelberg, Berlin, Heidelberg, pp. 51–86.
Wang, X., Zhao, Y.-P., 2020. The time-temperature-maturity relationship: a chemical kinetic model of kerogen evolution based on a developed molecule-maturity index. Fuel 278, 118264. https://doi.org/10.1016/j.fuel.2020.118264.
Warr, L.N., Cox, S.C., 2016. Correlating illite (Kubler) and chlorite (Arkai) "crystallinity" indices with metamorphic mineral zones of the South Island, New Zealand. Appl. Clay Sci. 134, 164–174. https://doi.org/10.1016/j.clay.2016.06.024.
Warren, J.K., George, S.C., Hamilton, J., Tingate, P., 1998. Proterozoic source rocks: sedimentology and organic characteristics of the Velkerri Formation, Northern Territory, Australia. AAPG Bull. 82 (3), 442–463. https://doi.org/10.1306/1D9BC435-172D-11D7-8645000102C1865D.
Weaver, C.E., 1959. Possible uses of clay minerals in the search for oil. Clays Clay Miner. 8, 214–227. https://doi.org/10.1016/B978-0-08-009351-2.50024-6.
Worden, R.H., Griffiths, J., Wooldridge, L.J., Utley, J.E.P., Lawan, A.Y., Muhammed, D.D., Simon, N., Armitage, P.J., 2020. Chlorite in sandstones. Earth Sci. Rev. 204, 103105. https://doi.org/10.1016/j.earscirev.2020.103105.
Wu, Y.W., Yin, R.S., Li, C., Chen, D., Grasby, S.E., Li, T.F., Ji, S., Tian, H., Peng, P.A., 2022. Global Hg cycle over Ediacaran-Cambrian transition and its implications for environmental and biological evolution. Earth Planet Sci. Lett. 587, 117551. https://doi.org/10.1016/j.epsl.2022.117551.
Xiao, J., Li, Z., Liu, B., Xia, Q., Yu, M., 2008. Adsorption of benzothiophene and dibenzothiophene on ion-impregnated activated carbons and ion-exchanged Y zeolites. Energy Fuel. 22, 3858–3863. https://doi.org/10.1021/ef800437e.
Xiao, Q.L., Sun, Y.G., Zhang, Y.D., 2010. The role of reservoir mediums in natural oil cracking: preliminary experimental results in a confined system. Chin. Sci. Bull. 55, 3787–3793. https://doi.org/10.1007/s11434-010-4178-0.
Xu, Q., Zhu, Y., Chen, S., Liu, Y., George, S.C., 2024. Organic matter accumulation as a convergence response to astronomical forcing: Insights from Milankovitch periods and sea-level fluctuations during the early Cambrian. Mar. Petrol. Geol. 163, 106812. https://doi.org/10.1016/j.marpetgeo.2024.106812.
Xu, R., Fazio, G.C., Matsuda, S.P.T., 2004. On the origins of triterpenoid skeletal diversity. Phytochemistry 65, 261–291. https://doi.org/10.1016/j.phytochem.2003.11.014.
Yan, J.F., Men, Y.P., Sun, Y.Y., Yu, Q., Liu, W., Zhang, H.Q., Liu, J., Kang, J.W., Zhang, S.N., Bai, H.H., Zheng, X., 2016. Geochemical and geological characteristics of the Lower Cambrian shales in the Middle-upper Yangtze area of South China and their implication for the shale gas exploration. Mar. Petrol. Geol. 70, 1–13. https://doi.org/10.1016/j.marpetgeo.2015.11.010.
Yang, B., Steiner, M., Li, G., Keupp, H., 2014. Terreneuvian small shelly faunas of east Yunnan (South China) and their biostratigraphic implications. Palaeogeogr. Palaeoclimatol. Palaeoecol. 398, 28–58. https://doi.org/10.1016/j.palaeo.2013.07.003.
Yao, L.P., Zhong, N.N., Khan, I., Chen, J., Luo, Q.Y., Zhang, Y., Ai, J.Y., Sun, W., 2021. Comparison of in-source solid bitumen with migrated solid bitumen from Ediacaran-Cambrian rocks in the Upper Yangtze region, China. Int. J. Coal Geol. 240, 103748. https://doi.org/10.1016/j.coal.2021.103748.
Yuan, G.H., Cao, Y.C., Schulz, H.M., Hao, F., Gluyas, J., Liu, K.Y., Yang, T., Wang, Y.Z., Xi, K.L., Li, F.L., 2019a. A review of feldspar alteration and its geological significance in sedimentary basins: from shallow aquifers to deep hydrocarbon reservoirs. Earth Sci. Rev. 191, 114–140. https://doi.org/10.1016/j.earscirev.2019.02.004.
Yuan, G., Cao, Y., Zan, N., Schulz, H.M., Gluyas, J., Hao, F., Jin, Q., Liu, K., Wang, Y., Chen, Z., Jia, Z., 2019b. Coupled mineral alteration and oil degradation in thermal oil-water-feldspar systems and implications for organic-inorganic interactions in hydrocarbon reservoirs. Geochem. Cosmochim. Acta 248, 61–87. https://doi.org/10.1016/j.gca.2019.01.001.
Zavitsas, A.A., 2003. The relation between bond lengths and dissociation energies of carbon-carbon bonds. J. Phys. Chem. A 107, 897–898. https://doi.org/10.1021/jp0269367.
Zhang, S., Zhang, B., Bian, L., Jin, Z., Wang, D., Chen, J., 2007. The Xiamaling oil shale generated through Rhodophyta over 800 Ma ago. Sci. China Earth Sci. 50, 527–535. https://doi.org/10.1007/s11430-007-0012-1.
Zhang, T., Peng, P.a., Li, Y., Sun, S., Guo, H., Pang, H., 2024. Molecular and carbon isotopic evidence for the possible origin of 13α (*n*-alkyl)-tricyclic terpanes in Mesoproterozoic bitumens from the Yanliao Rift, North China. Org. Geochem. 190, 104766. https://doi.org/10.1016/j.orggeochem.2024.104766.
Zhao, T.X., Xu, S., Hao, F., 2023. Differential adsorption of clay minerals: implications for organic matter enrichment. Earth Sci. Rev. 246, 104598. https://doi.org/10.1016/j.earscirev.2023.104598.
Zhao, W.Z., Hu, S.Y., Wang, Z.C., Zhang, S.C., Wang, T.S., 2018. Petroleum geological conditions and exploration importance of Proterozoic to Cambrian in China. Petrol. Explor. Dev. 45, 1–14. https://doi.org/10.1016/s1876-3804(18)30001-6.
Zhu, M.Y., Sun, Z.X., Yang, A.H., Yuan, J.L., Li, G.X., Zhou, Z.Q., Zhang, J.M., 2021. Lithostratigraphic subdivision and correlation of the Cambrian in China. Stratigraphy 45, 223–249. https://doi.org/10.19839/j.cnki.dcxzz.2021.0022 (in Chinese).
Zhu, M.Y., Yang, A., Yuan, J., Li, G., Zhang, J., Zhao, F., Ahn, S.Y., Miao, L., 2019. Cambrian integrative stratigraphy and timescale of China. Sci. China Earth Sci. 62, 25–60. https://doi.org/10.1007/s11430-017-9291-0.
Zhu, M.Y., Zhang, J., Li, G., 2001. Sedimentary environments of the early Cambrian Chengjiang biota: sedimentology of the Yu'anshan Formation in Chengjiang County, eastern Yunnan. Acta Palaeontol. Sin. 40, 80–105.
Zhu, X.J., Cai, J.G., Song, G.Q., Ji, J.F., 2015. Factors influencing the specific surface areas of argillaceous source rocks. Appl. Clay Sci. 109, 83–94. https://doi.org/10.1016/j.clay.2015.02.016.